**The Thesis Committee for Samuel Alexander Murphy**
**Certifies that this is the approved version of the following Thesis:**


**Study of Two-Photon Line Excitation Array Detection Microscopy**


**APPROVED BY**

**SUPERVISING COMMITTEE:**



Adela Ben-Yakar, Supervisor



Sudip Mondal

# Study of Two-Photon Line Excitation Array Detection Microscopy

**by**

**Samuel Alexander Murphy**

## Thesis

Presented to the Faculty of the Graduate School of

The University of Texas at Austin

in Partial Fulfillment

of the Requirements

for the Degree of

**Master of Science in Engineering**

**The University of Texas at Austin**

**May 2023**

# Acknowledgements

I would like to first thank my advisor, Dr. Adela Ben-Yakar, for her guidance and funding in support of this research. Thank you also to my wonderful lab colleagues, Berk Çamli, Andrew DuPlissis, Khashayar Moshksayan, Ani Harihara, Biswajit Mishra, Aditya Roy, and Daniel Wu, all of whom have either contributed directly to the project or spent precious time troubleshooting various obstacles with me. In particular, I would also like to acknowledge the mentorship provided by lab alumni Liam Andrus, Nicholas Watson, and Christopher Martin, who helped me in my research endeavors even after graduating themselves. Finally, I want to sincerely thank my parents, my partner Ross Pousson, my friends Rox Sayde, Jenna Montague, Katy Wong, and my dog Spartacus for providing me with abundant encouragement and emotional support throughout this process.

# Abstract

## Study of Two-Photon Line Excitation Array Detection Microscopy

Samuel Alexander Murphy, M.S.E.

The University of Texas at Austin, 2023

Supervisor: Adela Ben-Yakar

The functional meaning associated with neuronal activity in the mammalian brain is an active area of research limited by the available microscope instrumentation. Exploring this domain of neuroscience necessitates high-speed 3D imaging operating over 1 kHz volumetric scan rates with sub-cellular resolution, as action potentials propagate on sub-millisecond time scales. Monitoring these signals requires *in vivo* experimentation, so additional care must be taken to avoid invasive methods that may damage sample tissue to live animal subjects. Multi-photon imaging provides an opportunity for non-invasive microscopy with optical sectioning while simultaneously deeply penetrating brain tissue. However, current multi-photon microscopy methods are limited to 10-100 Hz volumetric imaging rates. This thesis explores and expands upon a potential high-speed 2-photon imaging technology, 2-photon Line Excitation Array Detection (2p-LEAD) microscopy. 2p-LEAD combines line scanning with detection via a multi-channel photomultiplier tube (PMT) array, with the potential to operate at 125 kHz frame rates.

In the experimental prototype outlined in this thesis, a 1035 nm excitation line of 2.4 µm x 259 µm (1/e2 beam intensity diameter) is scanned at the focal plane. The resulting fluorescence is collected by a 16-channel linear PMT array. With a fast-scanning galvanometric mirror, we scan the excitation line at 3,000 FPS, generating a 170 µm x 75 µm fluorescence FOV imaged to a 16 x 320 pixel frame. Temporal focusing was implemented to improve optical sectioning and signal-

to-noise ratio (SNR), by reducing the out of focus fluorescent signal. This reduction was achieved by dispersing the pulse-width from 300 fs at the focus to multiple picoseconds. 0.5-2 µm fluorescent polystyrene beads were imaged to characterize the system resolution of 1-5.3 µm laterally. Thus this research lays the groundwork for 2p-LEAD imaging at 125 kHz, with an acousto-optic deflector replacing the galvo-mirror as the primary scanning element, for high-speed neuronal imaging.

# Table of Contents

# List of Figures

# Chapter 1: Introduction

Research across many scientific disciplines is enabled through optical imaging technologies. In particular, microscopy has allowed doctors and researchers to visualize biologic activity on the cellular level non-invasively, providing key insight into the inner-workings of biologic processes. The underlying principle of microscopy uses the interaction of light with sample tissue to collect a signal, which can then be distinguished from the background of a sample to create an image [1]. These imaging systems are characterized by their signal to noise ratio (SNR), ability to distinguish fine characteristics (resolution), their speed, and their field of view (FOV). Primary forms of fluorescence microscopy include optical coherence tomography (OCT) [2], Raman spectroscopy [3], fluorescence microscopy [4], fluorescence lifetime imaging microscopy (FLIM) [5], and the subject of this thesis: multiphoton imaging, which has emerged as a standard method for non-invasive imaging [6].

Expanding the high-speed capabilities of multiphoton microscopy has the potential to broaden the scope of neuroscience research. Neural signals propagate in the form of action potentials. Action potentials are a cascading change in voltage throughout a neuron, where the negative resting voltage becomes more positive by allowing positively charged ions (mostly sodium and potassium) to enter. These potentials develop on the millisecond time scale while travelling comparably short distances within and between cells only 10-20 µm in length [7]. Understanding the information conveyed by the paths of action potentials in small clusters of neurons called "neurocircuits" is an active area of research with far-reaching implications throughout neuroscience [8]. Currently, genetically encoded calcium indicators (GECIs)- molecules which bond to $Ca^{+2}$ ions, whose distribution has a secondary association with action potentials- are the current standard fluorescent indicators used to track action potentials, and they activate ~50 ms. Their large activation time limits the accuracy of experimentation, being over an order of magnitude larger than the propagation speed of action potentials [7]. However, the recent development of genetically encoded voltage indicators (GEVIs) points to the possibility of

millisecond-scale action potential tracking in the near future [9]. To properly image these signals, a high-speed microscope that operates with the sub-cellular resolution is needed. In addition, since these signals require *in vivo* monitoring, this limits the fluence and resulting fluorescence intensity that can be collected, generating a situation with low photon counts. Though the optical sectioning capabilities of multiphoton imaging have proven effective for *in vivo* brain imaging, balancing the resolution and signal demands has traditionally been unattainable in multiphoton microscopy at high speeds [10]. Operating at high speed is achieved most easily by reducing the FOV and resolution, since it reduces the number of samples that must be acquired to form an image. Consequently, this often lowers the SNR, as less time is spent collecting light before forming an image as well. A new multi-photon imaging modality is thus required to perform this neuroscience research, which we explore in this thesis.

## 1.1: DISSERTATION OVERVIEW

The overall aim of this thesis is to demonstrate the feasibility of a new high-speed volumetric multiphoton imaging system for *in vivo* neural imaging.

Chapter 2 explains important background regarding the physical mechanism underlying fluorescence microscopy. It also explores important engineering constraints as well as the current methods for high-speed fluorescence microscopy and their limitations.

Chapter 3 presents a proposed method for high-speed multiphoton microscopy: two-photon line excitation array detection (2p-LEAD) microscopy. The chapter begins by outlining the design methodology and improvements made to the 2p-LEAD prototype. It then verifies the efficacy of the method by characterizing the system and evaluating images taken at 3,000 frames per second (fps).

Chapter 4 provides conclusions from the 2p-LEAD prototype design and outlines future work to allow the system to operate at >1,000 volumes per second.

# Chapter 2: Background

This chapter introduces the principles underlying fluorescence microscopy, associated instrumentation, and current high-speed microscopy.

## 2.1: MULTIPHOTON EXCITATION THEORY

Two-photon excitation is a unique extension of fluorescence that provides superior optical sectioning capabilities. General fluorescence occurs when incident light excites the electrons in a molecule to a higher energy state (**Figure 2.1**). When the electrons relax and return to a ground state, they then release energy in the form of light. Since there is often a range of excitation and relaxation states with various probabilities, the absorption and emission wavelengths of fluorescent compounds exist on a spectrum. Within these spectrums, the central emission wavelength is generally larger than the excitation wavelength, dubbed the Stokes' Shift, due to vibrational relaxation that occurs before emission, which reduces the emission energy [11].
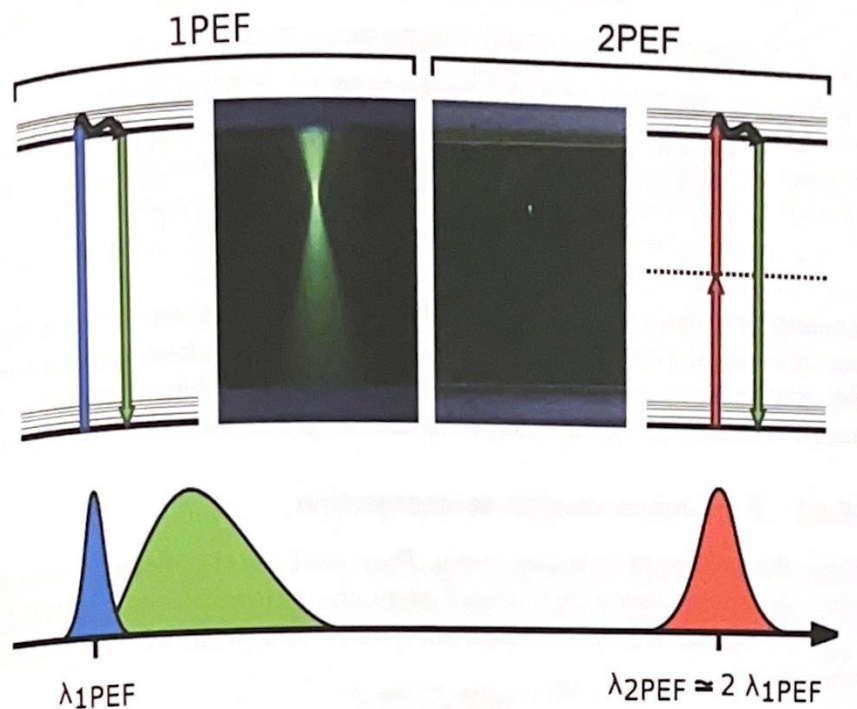


**Figure 2.1:** **Single and multi-photon fluorescence diagram.** 1 photon fluorescence on the left is compared to two-photon fluorescence on the right, with the two-photon

fluorescence exhibiting much stronger localization within the dye. At the edges of the figure are Jablonski diagrams, illustrating the relative energy of the excitation and emission in one and two-photon fluorescence. A comparison of the wavelength magnitudes is included below to illustrate the degree of difference between the one-photon and two-photon excitation light. Image taken from textbook *Fundamentals of Biomedical Optics*.

While fluorescent imaging proves quite effective for thin samples, in thicker samples, one-photon fluorescence can excite tissue outside the plane of interest, creating out of focus signal that makes an image difficult to resolve. Two-photon fluorescence reduces the out of focus signal by creating conditions that make it more difficult to excite tissue outside of the focal plane [6]. Originally hypothesized by Maria Göppert-Mayer in 1931, two-photon fluorescence occurs when two photons interact with the same fluorophore, and induce near-simultaneous excitement [12]. This dual excitement generates the same electronic excitation that would have occurred with one photon of half the wavelength. Since these photons need to excite within $10^{-16}$ s of each other, the photon concentration of excitation beam must be incredibly dense. This only occurs when a beam is tightly focused both spatially and temporally with high pulse energy, since the absorption probability is now dependent on the beam intensity squared based on the following relationship [13]:

$$\eta_{abs} = \frac{P^2 \delta}{\tau_P f_P^2} \left( \frac{A^2}{2\hbar c \lambda} \right)^2 \tag{2.1}$$

Where $\delta$ is the two-photon absorption cross section, which is generally estimated at $10^{-50}$ cm$^4$*s/photon (1 GM) [14]. Thus, out of focus planes where the beam is spatially dispersed produce little fluorescence, strongly reducing the background signal and improving optical sectioning.

## 2.2: TEMPORAL FOCUSING

Temporal focusing enhances the sectioning capabilities of two-photon imaging by providing an additional layer of dispersion outside the focal plane. In a typical optical microscopy system, the pulse-width of the excitation signal remains constant throughout the system. In 2005, it was discovered that the pulse-width of a laser, like its spatial component, could also be focused

by a microscope objective [15]. When a beam is focused onto a diffraction grating before the objective, the beam is spatially dispersed due to the dependence of wavelength on diffraction angle. In addition, we note that there is a temporal dependence on the incoming amplitude expressed as:

$$A(x,t) = \int_{-\infty}^{\infty} e^{-\frac{(x-\alpha\Delta\omega)^2}{s^2}} * e^{-\frac{\Delta\omega^2}{\Omega^2}+i\Delta\omega t} d\Delta\omega \tag{2.2}$$

Where $\sqrt{2\ln(2)}$ * s is the beam FWHM without dispersion, $\Delta\omega$ is the offset frequency from the central wavelength, $\Omega$ is the FWHM temporal bandwidth based on the input pulse width, and $\alpha$ is a proportionality constant. This relationship implies a temporal element to the dispersion passing through the diffraction grating. Performing a Fourier transform, multiplying by the spatial dispersion relationship $\exp(ikx^2/2f)$, and then performing an inverse transform, we are left with the following expression for the pulse width FWHM:

$$\tau(z) = \frac{1}{\sqrt{Re\left(\frac{1}{m}\right)}} * \frac{2\sqrt{2\ln(2)}}{\Omega} \tag{2.3}$$

Where z is the distance from the objective, and m is a complex function dependent on the objective working distance (f), z, s, $\Omega$, the wave number (k), and $\alpha$. The direct relationship of the pulse width and the distance from the objective working distance causes the pulse-width to broaden away from the focal plane by multiple orders of magnitude. This makes multiphoton excitation outside of the focal plane much more difficult, as it becomes less likely for multiple photons to simultaneously excite a fluorophore when they exhibit such low temporal density. As a result, the background fluorescence drastically decreases [16].

## 2.3: TYPICAL FLUORESCENCE MICROSCOPE DESIGN

The technology of 2p-LEAD utilizes multiphoton fluorescence microscopy, so a brief summary of common design considerations in single photon and multiphoton fluorescence systems is provided to better understand the research.

## 2.3.1: SOURCES FOR MULTIPHOTON MICROSCOPY

As discussed in the temporal focusing section, high pulse energies are needed in addition to strong spatial and temporal focusing to pack photons densely enough for two-photon interaction to occur. Two-photon fluorescence generally begins to occur with an incident fluence rate on the order of $GW/cm^2$. These energies are unattainable for long pulse durations, and will induce tissue damage, preventing *in vivo* imaging (**Figure 2.2**) [17]. Reaching these powers without photothermal effects or ablation requires a lower average power, with high peak powers, which are obtained through ultrashort laser pulses $< 1$ ps [18]. These short pulses allow low energy pulses to have the same effect as higher energy pulses $> 1$ ps, since the photons are so temporally concentrated. At the same time, since the energy applied is so low, the energy is able to dissipate quickly within the tissue without causing damage.
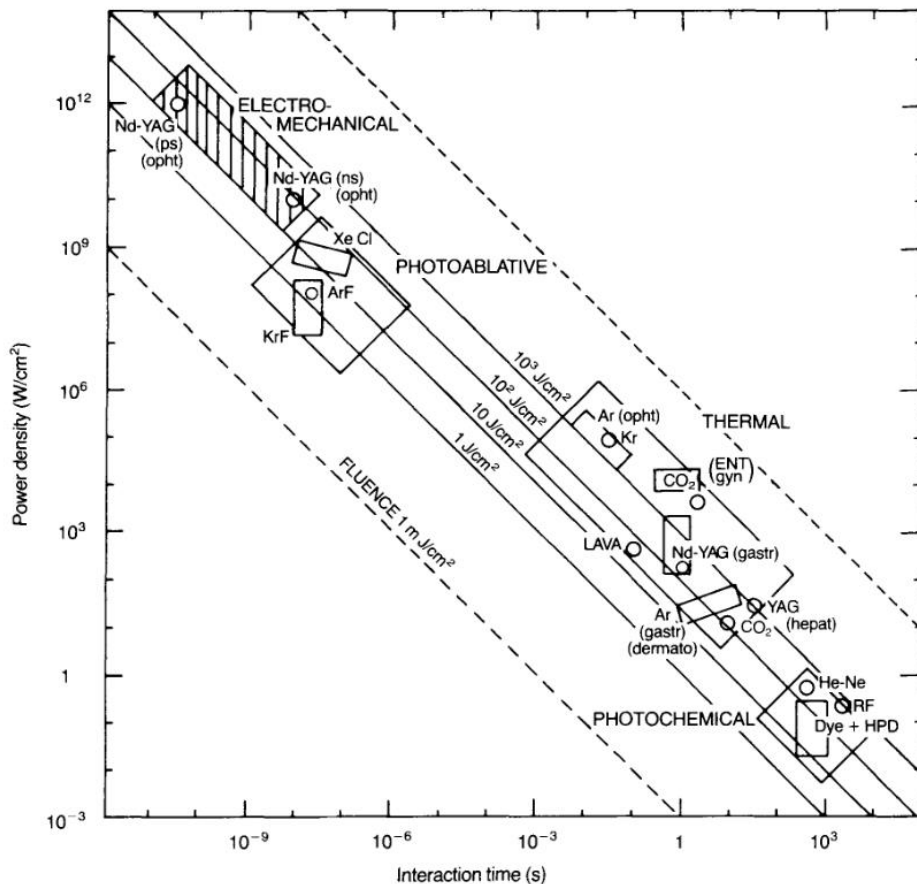
**Figure 2.2:** **Summary of types of laser-induced tissue damage.** Graph displays fluence rate and pulse duration necessary to induce different damage types, in addition to the lasers operating in a given regime. Below the 1 J/cm$^2$ line, damage is very unlikely to occur. Image taken from Boulnois review paper [18].

For multiphoton imaging at high speed, high repetition rates in the MHz range are also needed to acquire sufficient data. Each pulse of the laser excites additional data to be collected by the microscope, so the repetition rate directly scales with how fast information can be acquired. These repetition rate requirements inform the power of the laser source. To maintain low average power, the pulse energy needs to be reduced as the repetition rate is scaled up. A balance must be created in the system design so the peak power at high repetition rates remains large enough to induce multiphoton excitation, while maintaining a low enough average power to prevent tissue damage.

2.3.2: SCANNING METHODS FOR FLUORESCENT MICROSCOPY

One of the primary methods of image formation in fluorescent microscope systems is scanning a beam throughout a field of view to excite different portions of a sample. Three primary scanning methods exist: point scanning, line scanning, and random-access scanning (**Figure 2.3**) [19]. In point scanning, the excitation beam is focused to a point, and moved in two dimensions throughout a frame sequentially. Line scanning operates under a similar principle, but the excitation beam is instead focused to a line, requiring the beam to scan only along one access to form a full frame image. Finally, random-access scanning identifies regions of interest (ROIs), and then takes many randomly sampled data points in this small region, yielding high resolution. Each of these methods holds their own advantages and disadvantages. The highly localized point scanning beam creates good optical sectioning, but is more time consuming when generating image formation. While line scanning can be performed more quickly, the size of the line makes the excitation beam more vulnerable to scattering, and can reduce SBR as the signal is less localized [16]. Random-access scanning maintains the sectioning capabilities of point scanning

while enabling higher speed imaging with good resolution, but it fails to generate a true image [20]. In addition, locating ROIs can pose their own limitations to the imaging speed of the system [21].
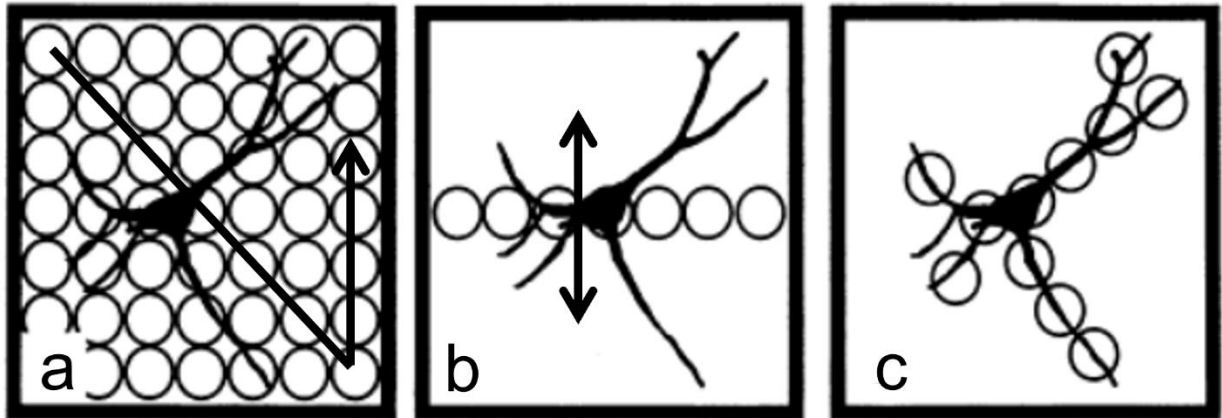


**Figure 2.3:** **Summary of laser scanning methods.** a) Shows an example of a raster scanned system, with each laser pulse corresponding to a scanned dot. b) Line scanning in one direction across a FOV. Each laser pulse generates one iteration of the line, and the collection system samples the line with a resolution corresponding to each diagram circle. c) Demonstrates random-access scanning of a neuron, taken to be the ROI. Image taken from Bullen review paper [19].

Laser scanning can be achieved through a multitude of methods, broadly split into mechanical scan methods, electro-optical scanning, and acousto-optic deflection. Mechanical scan methods are the traditional method of choice, where a reflective element is moved to deflect the excitation beam across a range of angles, scanning the beam at the sample perpendicular to the optical axis. Common mechanical scanning elements include polygonal mirrors, where each of the faces of the polygon scans the mirror as the polygon is rotated up to 70,000 rpm, and galvanometric mirrors, which use a servo motor to oscillate a single face flat mirror from side to side at < 10 kHz [22]. Galvanometric mirrors can also be resonant, which limits them to one frequency of operation, but increases their speed up to 24 kHz. Polygonal mirrors maintain constant speed, but have a fixed line scan and only operate in rotation, making them ill-suited for random access scanning. Though galvanometric mirrors exhibit more flexibility in scan range and speed, their scanning behavior is not uniform and- like all mechanical scanning systems- are inertia limited.

Electro-optical and acousto-optic scanning methods enable faster scanning as they are not inertia limited. Electro-optical elements can be electrically tunable lenses (ETLs) and electrically tunable mirrors, which operate by changing their index when a voltage is applied, thus changing the focusing power of the element and scanning the beam along the optical axis. These elements have response times < 1 ms, but much larger settling times that increase with lens thickness and aperture size [23]. Acousto-optic deflectors (AODs) instead use sound waves to deflect a beam and induce scanning by introducing local variations in the index of refraction, similar to ETLs. These AODs are controlled by a transistor, and their operation is controlled by the ultrasonic and mechanical properties by the relationship [24]:

$$Q = \frac{2\pi\lambda L f^2}{n_0 c_s^2} \tag{2.4}$$

Where $\lambda$ is the incident wavelength, L is the AOD thickness, f is the ultrasound frequency, $n_0$ is the nominal index of refraction, and $c_s$ is the speed of sound. The parameter Q helps identify what deflection regime the AOD is operating in: Raman-Nath regime (Q << 1) where the beam is deflected into a diffraction pattern, or Bragg regime (Q >> 1) where the beam is deflected into a specific diffracted order. Most scanning AODs operate in Bragg regime, with the scanning controlled by the equation:

$$\sin(\theta_B) = \frac{\lambda f}{2n_0 c_s} \tag{2.5}$$

Where $\theta_B$ is the Bragg angle, which corresponds to the +1 diffractive order for a given angle of incidence. Changing the ultrasound frequency applied by the transducer thus changes the scan angle of the AOD. The operating frequency of the AOD is limited by the time it takes for the wave to propagate along the length of the AOD ($\tau_R$) called the "access time", $\tau_R \sim w/c_s$. This propagation can either occur in the shear direction (shear mode) or longitudinal direction (longitudinal mode). Generally longitudinal mode operates the fastest, with access times low enough the AODs may operate ~100 MHz.

### 2.3.3: COLLECTION NOISE

In addition to the scanning method, the detection system used in a microscope has a great impact on the speed and accuracy of image reconstruction. The primary method of detection relevant to high-speed imaging takes advantage of the photoelectric effect, where incident light causes the ejection of an electron, or displacement of an electron to the conduction band of a material. Displacing the electrons in a material creates a positive charge the enables the flow of current in a detection circuit. The magnitude of the current response is directly proportional to the power of the incident light on the detector, allowing different features in a fluorescent system to be distinguished based on the magnitude of their emission.

The efficacy of this detection is dependent on many characteristics of the detector. The quantum efficiency ($\eta$) indicates the percent of incoming photons (power divided by expected energy per photon based on wavelength: $P/(h\upsilon/\lambda)$) which generate a charge response (Number of electrons displaced based on the current response: $I/e$) [25]. Quantum efficiency can thus be characterized by measuring the current response of the detector to a particular power and wavelength of energy incident on the detector:

$$\eta = \frac{Ih\upsilon}{P\lambda e} \tag{2.6}$$

This quantum efficiency informs the responsivity of the detector, which is the magnitude of the current response for a given incident power. The responsivity is generally wavelength dependent, and the full characterization of the responsivity based on wavelength is the detector's spectral response. Importantly, the relationship between the incident photons and electron counts of the detector are probabilistic. A quantum analysis shows that [26]:

$$(\Delta N)^2 = \eta^2(\Delta n)^2 + \eta(1 - \eta)\bar{n} \tag{2.7}$$

Where $(\Delta N)^2$ is the variance in the electron counts, $(\Delta n)^2$ is the variance in the photon counts, and n is the average number of photons. The probabilities are based on the natural fluctuations in the

photon density of a source. As η → 0, the detector response becomes a poisson process based on the mean photon count, which is highly probabilistic and not necessarily representative of the emission of a fluorescent system. However, as η → 1 the variance of the electron counts corresponds exactly to the variance in the incident photons. Thus the quantum efficiency determines not only the magnitude of the detector response to an incident beam, but also how accurately it captures the true power fluctuations. Other key factors impacting detection speed are the response time and bandwidth of the detector. The response time is the speed at which the detector can respond to changes in power, and the bandwidth of the detector is the frequency at which a detection signal diminished by 50%, allowing other signals to be detected [27]. A combination of high quantum efficiency to reduce dwell time, and fast response time and bandwidth are needed to achieve high-speed imaging.

Mitigating and managing detector noise is also important when designing imaging systems. Noise created by detectors can arise from many sources. Shot noise is a form of noise inherent in detection systems, and is a result of the quantum nature of the electronics. As is implied by equation [INSERT HERE], the shot noise scales with the square root of the incident signal and is roughly poisson distributed [28]. Thus as the signal intensity is increased, the relative magnitude of the shot noise decreases in comparison to the signal, improving the SNR. When thermal fluctuations and environmental factors produce current response without an incident signal, this constitutes dark noise [29]. Similarly, Johnson noise occurs when thermal effects cause the fluctuations in the load resistance of the detector circuits, impacting the current response. In all cases, steps can be taken to minimize the noise (operating in a cool temperature controlled area, minimizing stray light, using detectors with high quantum efficiency in the given wavelength range, etc.), but the presence of noise remains inherent to imaging. Combining all these factors together, SNR can be expressed as [30]:

$$SNR = \frac{\mu}{\sqrt{\sum_i^n \sigma_i^2}} \tag{2.8}$$

Where μ is the average signal, and $\sigma_i$ is the standard deviation of the associated noise. Ultimately, other noise sources are generally small, and shot noise is most commonly the limiting factor in imaging systems.

2.3.4: DETECTORS FOR FLUORESCENT SYSTEMS

Detection systems can operate either as an array or single-elements system. Common array detectors include complimentary semi-oxide conductor (CMOS) cameras and charge couple device (CCD) cameras. CCD cameras operate by generating potential wells of emitted electrons, where the electron well is filled through increasing photon counts [28]. The charge from the wells is converted an analog to a digital (ADC) signal, forming a pixel array that can be translated into an image. Though highly sensitive and efficient, the readout rates are quite slow ~ 0.1 s due to the shared ADC components for all potential wells. CMOS cameras offer improvements in read out speed by assigning each array element its own readout circuit, allowing information to be read and converted simultaneously across the wells at rates < 10 μs [31]. However, CMOS cameras are much less sensitive, have lower quantum efficiency, and are more susceptible to noise, necessitating long development times in low lights systems that can limit imaging speed and accuracy.

Single element detectors can offer better sensitivity and readout speeds at the expense of requiring a sample to be scanned. The simplest single element detector is the photodiode (PD), which consists of a p-doped semiconductor with extra holes, layered on an n-doped semiconductor with free electrons (**Figure 2.4**). The circuit is reverse biased, so the cathode is attached to the negatively charged n-doped semiconductor, while the PD circuit anode is attached to the p-doped semiconductor. A depletion region between the two semiconductors forms which is neutral and houses most of the charge carriers. Incident light lifts an electron to the conduction band of the depletion region via the photoelectric effect, which generates a current response that is normally blocked by the bias voltage. So past a certain threshold, the current response of the PD will scale with the power of incident light. In avalanche photodiode detectors (APDs), this bias voltage is

21

very large, providing additional energy to ejected charge carriers that amplify the current response. Silicon photomultipliers (SiPMs) use multiple APDs to further amplify the signal, for total gain up to $10^6$. As a result, APDs can detect single photons above the noise, though this method requires resetting that limits the detector bandwidth.
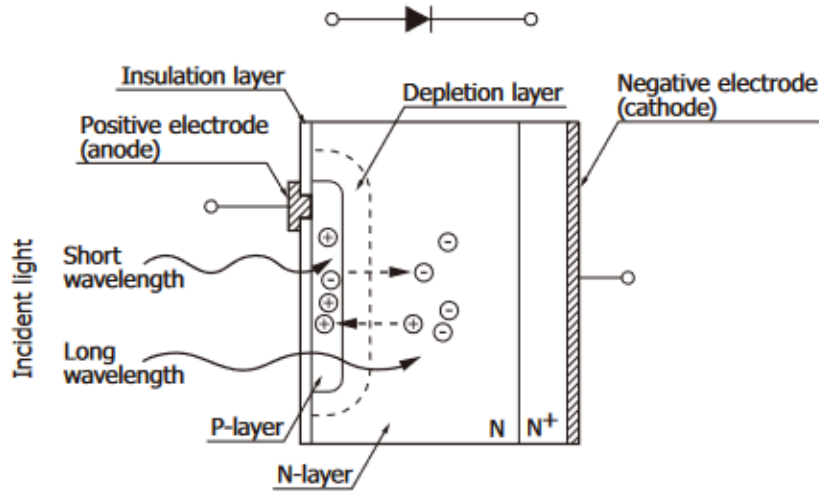


**Figure 2.4:** **Diagram of a typical photodiode.** Depletion region is shown between the p and n layer semiconductors, with the anode aligned with the p-layer and the cathode aligned with the n-layer creating reverse bias voltage. Incident light enters coming into the diagram, on the active area of the detector. Movement of charge carriers shows the positive charges leaving the n-layer and negative charges leaving the p-layer, effectively broadening the depletion layer. Image taken from Hamamatsu photomultiplier tube review [32].

Photomultiplier tubes (PMTs) are another class of single element detectors with improved bandwidth. PMTs operate by amplifying the ejection of electrons from a photocathode by incident light using dynodes, a series of secondary emissive materials that add additional electrons to the emission circuit on impact (**Figure 2.5**). These electrons are collected by an anode at the end of the dynode chain, and the difference between the anode and cathode voltage in the PMT circuit generates a current response. The dynode chain can amplify the current response by up to $10^8$, making PMTs exceptionally sensitive detectors that can also detect single photons like APDs. PMTs also exhibit low noise, which can be characterized by [33]:

$$SNR = \frac{i_c}{\sqrt{2eF_eB(i_c + 2i_d) + i_n^2}} \tag{2.9}$$

Where $i_c$ is the response current, $i_d$ is the PMT dark current, $i_n$ is the noise current, B is the circuit bandwidth, e is the electronic charge, and $F_e$ is the excess noise factor. The excess noise factor is determined based on the dynode secondary emission ratios ($\delta$), which characterize the amplification of the current at each dynode:

$$\delta = \frac{I_{dynode,out}}{I_{previous\ dynode}} = aE^k \tag{2.10}$$

Where a is a proportionality constant, E is the interstage dynode voltage, and k is a material structure constant. These secondary emission ratios determine the excess noise factor as well as the overall current amplification ($\mu$) of the PMT:

$$F_e = 1 + \sum_{i=1}^{n} \frac{1}{\prod_{j=1}^{i} \delta_j} \tag{2.11}$$

$$\mu = \alpha \prod_{i=1}^{n} \delta_i \tag{2.12}$$

Where $\alpha$ is the collection efficiency of the PMT. In addition to their high gain and relatively low noise, PMTs exhibit typical bandwidth of 100 MHz, though this may be reduced by the amplification electronics necessary to generate readable data. PMTs are thus uniquely suited to high-speed imaging in low photon count fluorescent systems. New PMT models are also creating PMT arrays, which reduce the scale of scanning necessary to image with these detectors.
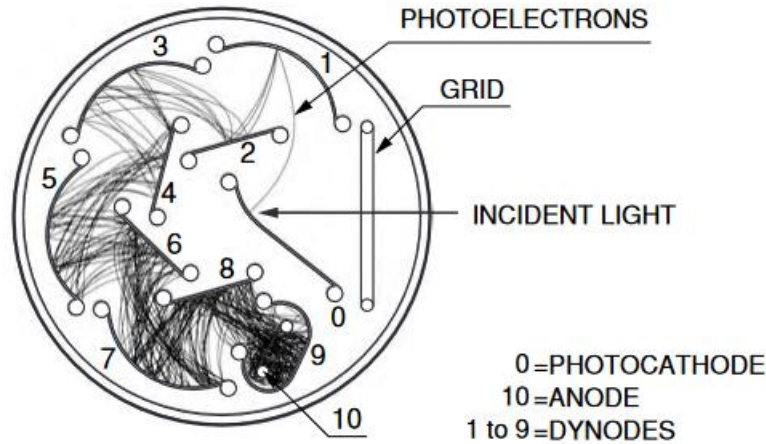
**Figure 2.5:** **Diagram of a circular cage type PMT.** The $0^{th}$ surface is the photocathode, which emits electrons when exposed to incident light via the photoelectric effect. The following surfaces are dynodes which amplify the free electrons passing through the system to the anode (surface 10). Differential between the photocathode and anode charge generates the current response of the detector. Image taken from Hamamatsu photomultiplier tube review [33].

## 2.3.5: FLUORESCENCE MICROSCOPY IMAGE CONSTRUCTION

Microscopy which uses scanning and single element detection requires extra characterization when forming an image. In fluorescence microscopy, the excitation beam that excites sample fluorophores has its own size, which impacts the signal and resolution obtained by the microscope at the detection plane. When imaging a point source or any features significantly below size of the excitation beam, the result will be the emitted beam size, called the point spread function (PSF) (**Figure 2.6a1**) [34]. An image formed with this system will be the result of the object convolved with the PSF, and will thus not exactly reflect the true sample for features larger than a point source. Extracting the true image requires taking the Fourier transform of the image and the PSF, called the optical transfer function (OTF), then performing a deconvolution to extract the object:

$$O = \mathcal{F}^{-1}\left\{\frac{\mathcal{F}\{I\}}{OTF}\right\} \tag{2.13}$$

24

Where I is the image signal and O is the true object signal. The resolution of the system is typically characterized based on the fit of the PSF, and represents the minimum spacing where two objects may be distinguished (**Figure 2.6a2,a3**). In a diffraction limited system, the resolution is dependent on the wavelength and system NA by:

$$r = \frac{0.61\lambda}{NA} \tag{2.14}$$

If the system is not diffraction limited the FWHM of the PSF is taken to be the resolution. Spot size, which is reduced in higher NA systems, thus directly impacts the resolution of a fluorescent imaging system.
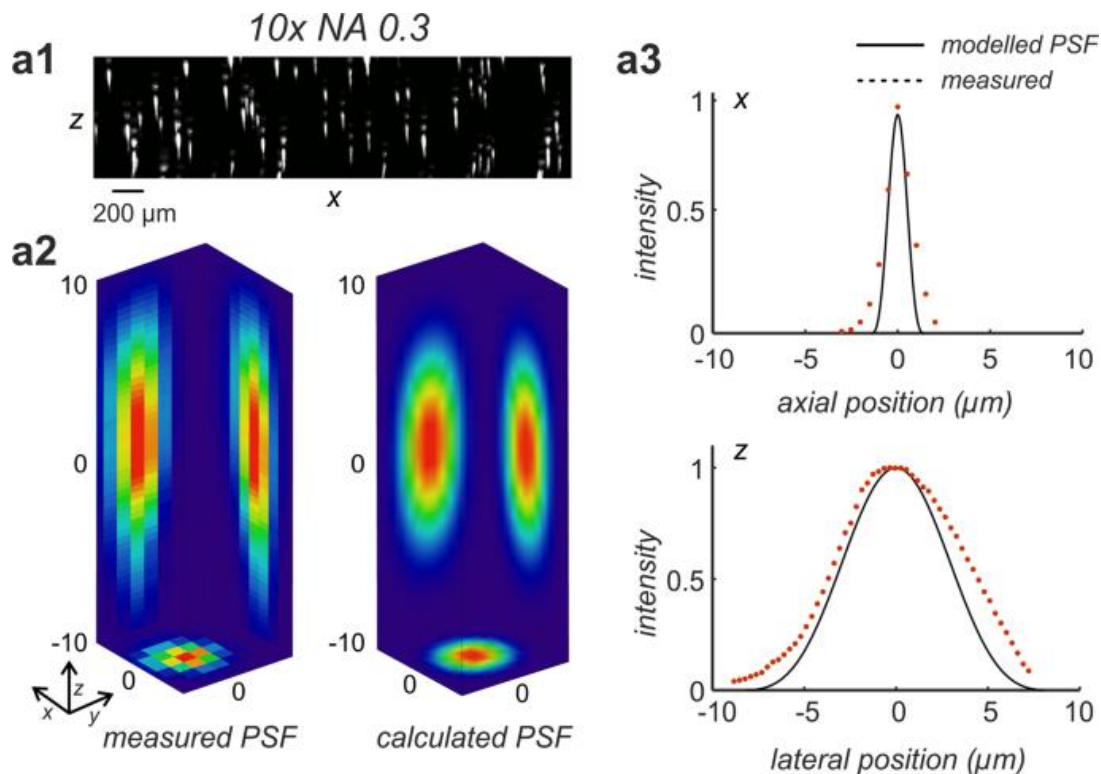


**Figure 2.6:** **Example PSF characterization in microscopy.** 200 µm fluorescent beads are imaged by a light sheet microscope to characterize its resolution. a1) Shows the raw image of the x-z cross-section for a given objective system. a2) Provides a close-up view of full x-y-z cross-section of one bead. a3) Shows the x and z dimension measured intensity in the image (red dots), and the PSF fit assigned to the data (black line). As the beads are much smaller than the resolution of the system, they act as point sources, so the resulting image does not require deconvolution to obtain the PSF. A bead imaging experiment such as this is extremely common for

characterizing the PSF and resolution of a microscope system. Image taken from Becker et. al. [34].

The resolution of an optical system can be further reduced by the presence of aberrations. Aberrations can be introduced by the optical elements and imaging conditions of a system, and can either distort the excitation or the collection beam in a fluorescent system. These aberrations can be identified by analyzing the OTF, as individual aberrations contribute particular distortions to the OTF shape (**Figure 2.7**). The order of an aberration indicates how the aberration severity scales with beam size. Tip/tilt and defocus are the only first-order aberrations and generally result from poor alignment [35]. Third order aberrations include spherical aberration, coma, and astigmatism, and fifth order aberrations include field curvature and distortion. Spherical aberration is caused by paraxial rays being focused more intensely by a lens than rays closer to the lens center, blurring the focal plane. Chromatic aberration is when this focal blurring occurs with different wavelengths focusing to different locations, due to the wavelength dependence of index in a system's optical elements. Coma results when off-axis rays are focused to different locations based on which section of a lens the rays pass through. Astigmatism occurs when the focusing power of a system is not uniform, causing different axes to focus at different locations of the optical axis. Astigmatism and coma can also be introduced with non-index matched materials such as coverslips in the microscope beam path. Field curvature occurs when the off-axis rays are not focused to the plane, causing a curved focal plane. Distortion arises from uneven magnification between the center and edges of an image. The presence of some aberration is unavoidable, but steps can be taken to minimize their impact on the microscope system. Spherical aberration and astigmatism can be mitigated by introducing defocus or using aspheric lenses. Specific lens pairs such as achromatic doublets also exist to correct for chromatic aberration. In addition, many microscope objectives are specifically designed to correct for chromatic aberration, field curvature, and other aberrations.
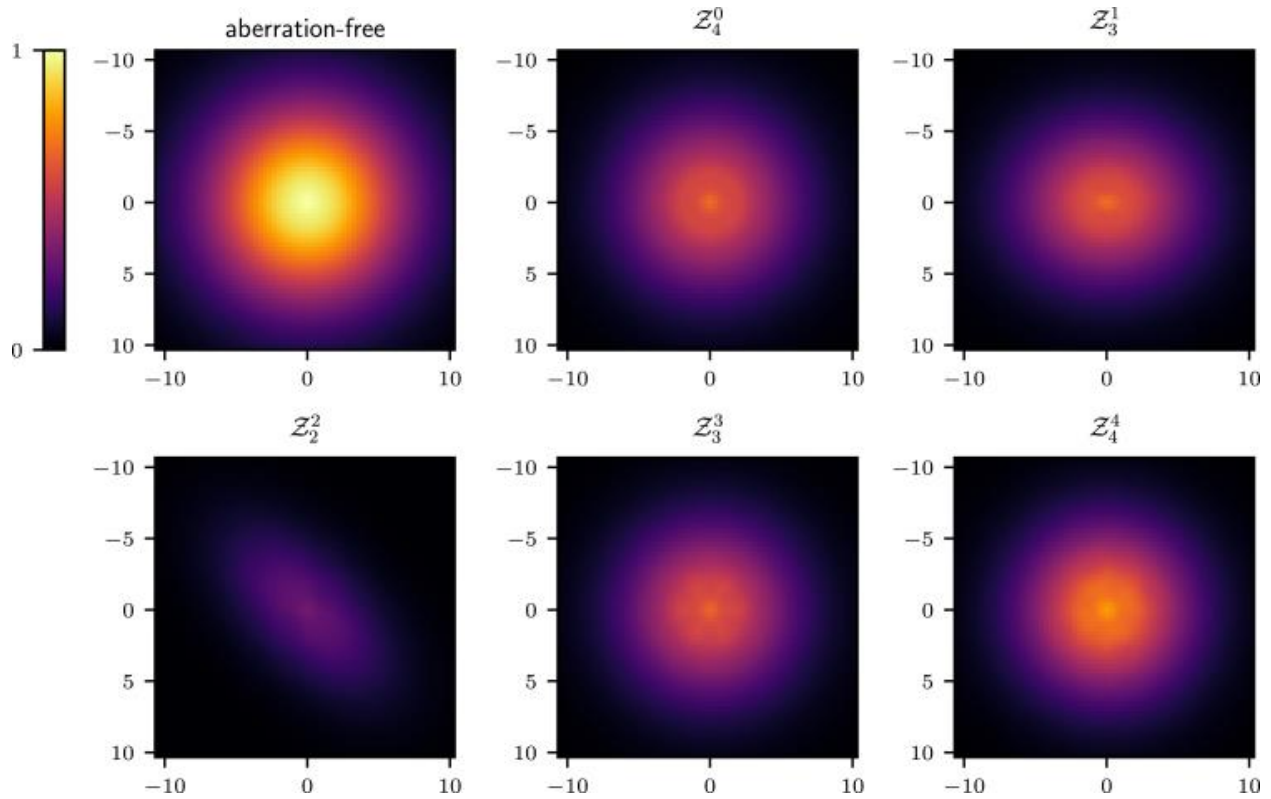
**Figure 2.7:**  **Illustration of OTF with different aberrations.** The upper left image represents an aberration free imaged spot OTF. The remaining OTF images are: Z04 spherical, Z13 coma, Z22 astigmatism, Z33 trefoil, and Z44 quadrafoil. Image is taken from Antonello et. al. [36].

## 2.4: CURRENT HIGH-SPEED FLUORESCENCE MICROSCOPES

Current microscope systems can be sorted into three main categories: wide-field fluorescence microscopes, confocal point-scanning or light-sheet microscopes, and two-photon point-scanning microscopes [37]. Almost all of these microscope types are epi-fluorescent. In an epi-fluorescent system the emission signal is imaged by the same objective that delivers the excitation beam to the sample. The emission signal is later directed to its own path by a dichroic mirror, which has a wavelength dependent reflectance/transmission spectrum. Light-sheet confocal microscopy is the only exception to this, which instead uses multiple objectives (**Figure 2.8c,g**). The first objective delivers the light-sheet to the sample, and a second objective is placed perpendicular to the first objective to capture the fluorescence from a different plane for collection.

Scanning the light-sheet or the sample allows a 3D image to be constructed. In comparison, wide-field fluorescence microscopy is much more limited. Wide-field fluorescence illuminates the whole image frame simultaneously, and images the full frame directly onto an array detector like a CMOS camera [38]. These microscopes are not capable of axial sectioning, and are ill-suited to low contrast samples, since background fluorescence can easily reduce SBR in thick samples. Thus these microscopes are limited to 2D imaging of thin or high contrast samples. In confocal fluorescence systems, sectioning is enabled by introducing a pinhole in the collection path (**Figure 2.8a,e,f**). The pinhole blocks rays from axial sections outside the focus, since their rays will have different slopes and sizes than the focused beam, thus allowing only emission from the focal plane to reach the detector. Confocal microscopes require a small emission beam to implement this pinhole blocking mechanism, so they generally use point-scanning with single element detection to build a full 3D image. Two-photon fluorescence microscopes operate similarly, but use multi-photon excitation to induce axial sectioning in place of the pinhole block (**Figure 2.8b,h**).
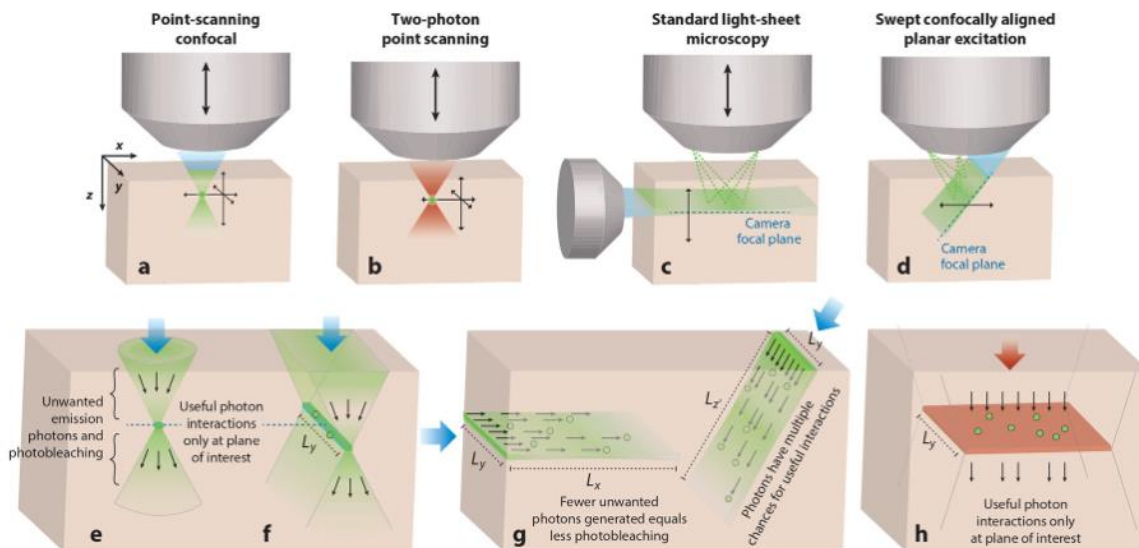


**Figure 2.8:** **Summary of common fluorescence microscopy systems.** In all diagrams, blue light and red light correspond to one-photon and two-photon excitation beams respectively. Green sections indicate fluorescence. Solid black arrows indicate the scan direction, and dashed lines indicate the focal plane. a) Demonstrates one-photon excitation in a sample of a point-scanning microscope. b) Shows two-photon excitation in a sample of a point-scanning microscope. c) Shows a standard

light-sheet microscopy system, with the imaging objective perpendicular to the light sheet excitation plane and camera plane. d) Shows SCAPE, a popular high-speed microscope which implements an oblique light sheet. e) Representation of emission volume in a point-scanning system. f) Representation of emission volume in a line-scanning system. g) Representation of fluorescence sheet with light-sheet excitation. Standard orientation is shown on the left, and oblique is shown on the right. In both cases, the volume is smaller and generates less photobleaching than the confocal scanning systems. h) Representation of fluorescence in a two-photon confocal scanning system. Fluorescence only appears sporadically at focal plane of interest, due to the low probability of two-photon emission compared to other fluorescence methods. Image taken from Hillman review paper [39].

Current microscope instrumentation is limited to well-below the kilohertz volumetric imaging rates needed to track neural circuits. High-speed wide-field fluorescent microscopes have been limited to ~1 kHz frame rates, in some cases due to the development time of the high speed camera used [40,41], and other times due to the inertial limitations of the mechanical scanners used to generate the wide-field beam [42]. These same limitations apply to forms of confocal microscopy [43]. Advancements in the imaging speed have been achieved through combination light-sheet and confocal scanning microscopy such as SCAPE 2.0, which can capture >300 VPS by imaging an oblique light sheet plane, so only one axis of scanning is necessary to create a 3D image [44]. Similar advancements have been made in two-photon point-scanning microscopy. Resonant galvanometric mirrors limit traditional two-photon imaging to ~10 VPS and frames rates >10 kHz [45]. Implementing random access imaging with acousto-optic deflectors as the primary scan mechanism has allowed two-photon point-scanning systems to operate up to 40 kHz frame rates [20]. As discussed in section 2.3.2, random-access scanning does not fully represent a sample, and also requires planned scanning regions that can reduce data acquisition time. Ultimately, improvements in the existing microscopic technology are still needed to properly image neural circuitry volumetrically at 1,000 VPS.

# Chapter 3: Two-photon Line Excitation Array Detection Microscopy

This chapter presents the design and results of a two-photon LEAD microscope. This includes the initial design, design improvements, microscope construction, characterization, and initial imaging with reference to the background established in chapter 2.

## 3.1: SYSTEM DESIGN

### 3.1.1: SYSTEM DESIGN OVERVIEW

To enable kilohertz volumetric imaging for neuroscientific research, 2p-LEAD technology was developed. 2p-LEAD is an extension of single-photon LEAD cytometry, which was previously developed to image c. elegans specimens at 0.8 million frames per second (**Figure 3.1**) [46]. The basic underlying principles of the two systems are the same: An excitation line is scanned in one dimension, and the resulting fluorescence is imaged onto a multi-channel PMT array, to directly image individual portions of the scanned line. In LEAD cytometry, the excitation beam is an oblique sheet and generates one-photon fluorescence response, and the fluorescence is imaged by a second objective perpendicular to the excitation line. Since the cytometer naturally flows the c. elegans worms, sample scanning is not necessary. In contrast, 2p-LEAD more closely mimics conventional microscope configurations by using epi-fluorescence, and requiring axial scanning to form a full 3D image. 2p-LEAD also takes advantage of two-photon emission and temporal focusing to improve axial sectioning, allowing signal to be recovered during deep tissue imaging in highly scattering media such as brain tissue. Like LEAD cytometry, the end-design of 2p-LEAD is to scan using an AOD in longitudinal chirped mode for >100 kHz scanning in the focal plane. This thesis explores the preliminary 2p-LEAD design using a scanning galvanometric mirror, which limits the system to 3 kHz frame rates, and provides additional insight to extend this technology with AOD scanning. This work includes reference to an initial 2p-LEAD model with a limited 17.9 µm x 27.1 µm FOV, a second iteration on this design to improve the FOV, and further design improvements that were made to improve the collection, SNR, and FOV as well.
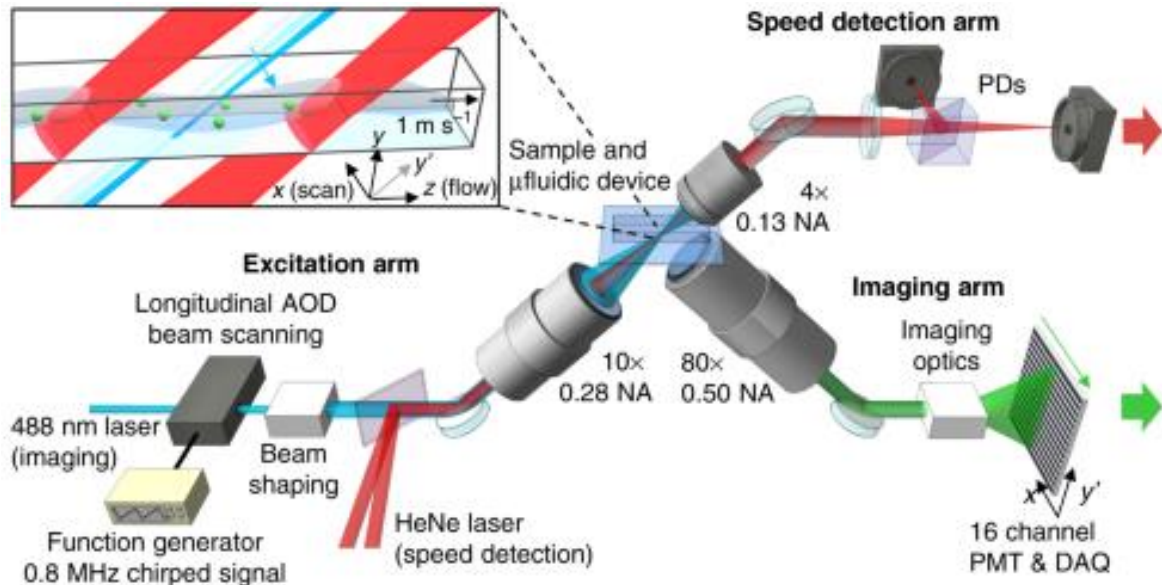
**Figure 3.1:** **Diagram of LEAD cytometer.** Included for comparison to the 2p-LEAD system. 488 nm (blue) and 632 nm (red) light are incident oblique light sheets in the y-z plane at the microfluidic sample. The 488 nm laser light is scanned in the x dimension by an AOD, and the flow of the c. elegans worms at ~1 m/s allows a full 3D image to be constructed. The HeNe laser light is detected by a pair of PDs to track the speed. A second objective images the fluorescence (green) from the c. elegans onto a 16-channel PMT array. Each dimension had a resolutions between 3-4 µm with a 60 µm x 50 µm FOV in the x-y plane. Image taken from the original LEAD cytometry paper [46].

### 3.1.2: EXCITATION ARM MODEL

As discussed in previous sections, two photon imaging is only possible when using high-intensity peak powers due to the $I^2$ dependence of fluorescence on the excitation signal. At the same time, high-speed imaging at 100 kHz frame rates requires a laser repetition rate in the ~10 MHz range to appropriately sample a frame. To satisfy these ends, we chose to use the 40W Monaco 1035 nm laser from Coherent Inc., which is one of the few lasers to boast a 50 MHz variable repetition rate at such high powers. The 1035 nm central wavelength is not traditionally used with 2-photon indicators, but we anticipate that the high peak power will compensate for this. The laser output was characterized using the APE PulseCheck autocorrelator, by rotating the laser to s-polarization and aligning the beam into the interferometer in a dark room. After obtaining the pulse autocorrelation (**Figure 3.2a**), a deconvolution was performed to extract the laser pulse-

31

width FWHM. A range of powers from 0.5 W – 7.0 W along with a set of repetition rates from 2 MHz to 50 MHz were sampled, effectively sampling pulse energies from 10 nJ - 3.5 µJ (**Figure 3.2b,c**). When the laser was set to output 300 fs pulses through its user interface, a pulse width of 340.8 ± 13.7 fs was observed for the 10 nJ pulse case, and a pulse width of 332.8 ± 6.8 fs for the 3.5 µJ pulse case. Indeed, these values remained relatively constant for the full range of pulse energies between repetition rates as well. The slight yet consistent average 36 fs increase from the set 300 fs pulse output indicates the presence of some temporal dispersion. However, the overall shape of the beam is consistently gaussian over the range of pulse energies, with no irregularities or wings what would create an uneven energy distribution at the sample. Both factors indicate that the laser can be effectively used at low or high pulse energies in our system, and we generally did not consider this a limiting factor when performing experiments, regardless of repetition rate.
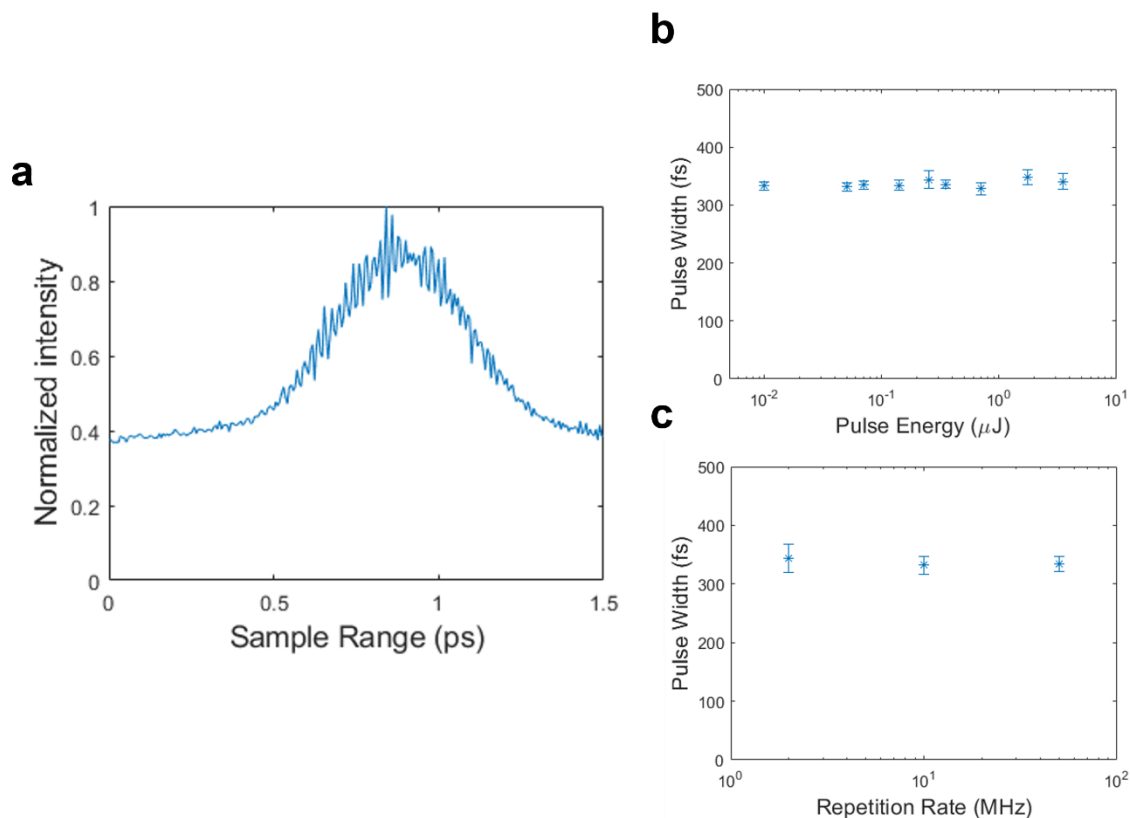


**Figure 3.2:** **Summary of laser pulse characteristics.** a) A sample autocorrelation data from the APE PulseCheck. b) Estimated FWHM pulse width as a function of pulse energy. No clear relationship was observed. c) Estimated FWHM pulse width as a function of laser repetition rate. No clear relationship was observed.

After choosing our laser, the rest of the excitation components were determined based on the desired properties at the sample plane. The first iteration of 2p-LEAD used a small excitation line of 2.0 µm x 22.2 µm ($1/e^2$ diameter in x and y), limiting the field of view in the y-dimension to the 22.2 µm linewidth. Since we want to image over a larger FOV, the theoretical line at the sample plane was increased to 2.6 µm x 257.4 µm ($1/e^2$ diameter) (**Figure 3.3**). The starting size of the laser beam is roughly 3.82 mm x 4.29 mm ($1/e^2$ diameter), and first encounters the galvomirror (ScannerMax Saturn 5B, 5mm aperture) which is controlled by a function generator and scans the beam at 3 kHz using a triangle wave. Then the beam is focused down to 43.1 µm x 3.82 mm ($1/e^2$ diameter) by a 125 mm focal length cylindrical lens in the x-dimension, forming a line. The cylindrical lens is placed 125 mm after the galvomirror so the lens images the beam before it is deflected through the scan. The line created by the cylindrical lens is focused onto a 1600 lines/mm transmission diffraction grating (ii-vi, T-1600-1030s), which introduces both spatial and temporal dispersion into the system. The diffraction grating is placed in the Littrow configuration, where the most efficient position of the grating moves >94% of the incident light into the +1 diffracted order at roughly the same angle as the incident angle. In this case, our grating was designed with a 55° Littrow angle based on the grating equation [47]:

$$Gm\lambda = \sin(\alpha) + \sin(\beta) \qquad (3.1)$$

Where G is the groove density, m is the diffracted order, α is the incident angle, and β is the diffracted angle. In addition, our grating is polarization sensitive. So, a twisted periscope was used before the galvomirror to rotate the beam from p to s-polarization, the most efficient polarization state for the grating, without interfering with the system's scanning. A conjugate plane is then made between the line focused onto the diffraction grating and the sample plane through a combination of optics. A 300 mm focal length spherical tube lens is placed 300 mm after the grating and the system's 10x 0.6 NA water immersion objective (Olympus) is placed 300 mm after the tube lens. The combination of the cylindrical lens and tube lens in this configuration creates a telescope system in x that magnifies the x-dimension of the beam to fill the objective back aperture,

while the tube lens focuses the beam in the y-dimension. This focusing condition causes the y-dimension beam to exit the objective roughly collimated, and the x-dimension to be tightly focused at the sample plane, generating a de-magnified version of the line incident on the diffraction grating at the sample. Since the rated tube lens for the objective is 180 mm, the de-magnification from the grating plane to the sample is $M = \frac{300\,mm}{180\,mm}10x = 16.67$, ultimately creating the desired sample line of 2.6 µm x 257.4 µm (1/e² diameter). Notably, this set of focusing conditions directs the beam onto the same position of the objective back aperture regardless of scan angle. Instead, the beam enters the objective at a different angle, which is what causes it to scan at the sample plane.
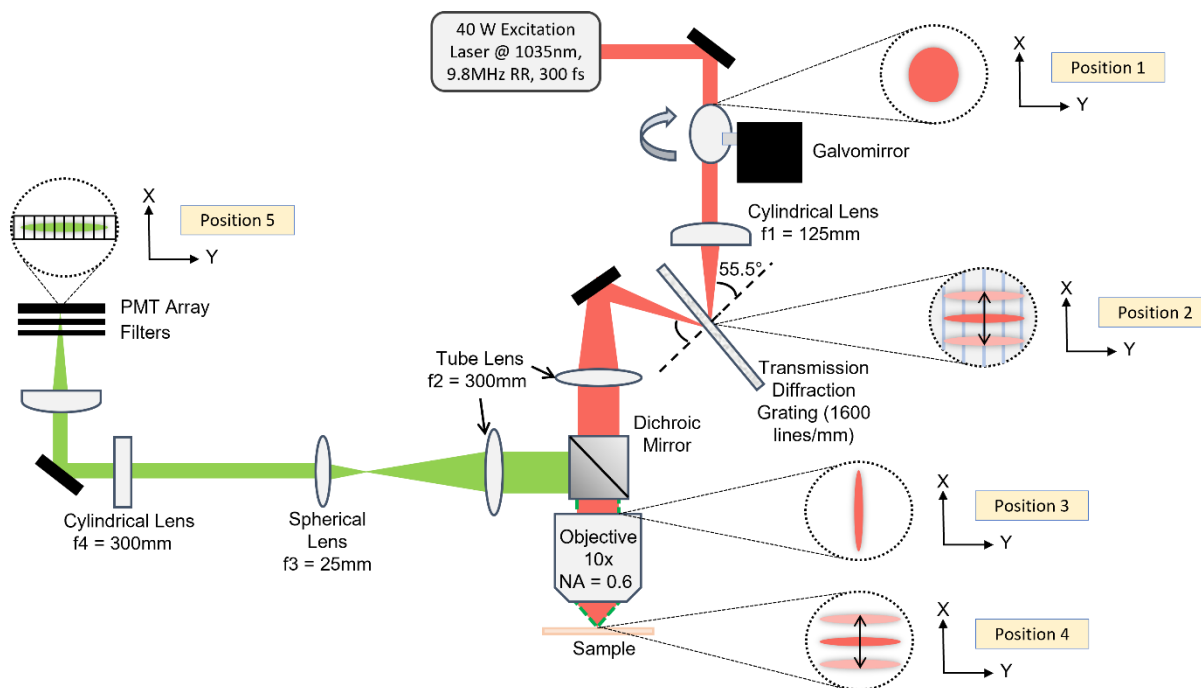


**Figure 3.3:** **Diagram of current 2p-LEAD system.** Shown is the x-z cross-section of the 2p-LEAD optical path, where the z-dimension is the optical axis, and the x-dimension is perpendicular. Pink blocks correspond to the excitation beam, and green to the emission beam. Key positions include x-y cross-sections of the beam to illustrate how the line develops throughout the system. Position 1 shows the beam exiting the laser and incident on the galvomirror. Position two shows the beam shaped to a line at the transmission diffraction grating. The lines in the background represent the grating grooves, which are oriented parallel to the x-dimension. Position 3 shows the beam at the objective back aperture, where it is focused in y and collimated to fill the BA in x. Position 4 is the beam at the sample plane, where the arrows indicate the scan direction in the x-dimension. Finally, position 5 shows the beam orientation and shape when collected onto the PMT array.

The theoretical values calculated assume no dispersion from the grating, which we know is not the case. Since our laser has a bandwidth of $\Delta\lambda = \pm 5$ nm FWHM, and the diffraction angle is wavelength dependent, the laser light passing through the diffraction grating will be diffracted at slightly different angles, introducing spatial dispersion. This dispersion changes the beam profile at the focal plane. To more accurately estimate the sample beam size, a simulated model of the excitation path was created in Zemax OpticStudio (**Figure 3.4a**). The simulation uses a 20X water immersion objective, since this is more well characterized. To adjust the results for our system, values from the Zemax simulations were multiplied by 2x to better reflect the expectations from the 10x objective in 2p-LEAD. Based on this model we expect a 2.4 µm x 258.4 µm ($1/e^2$ diameter) beam at the sample when using the diffraction grating for temporal focusing (**Figure 3.4b**). Implementing temporal focusing surprisingly generated little change in the beam size at the sample plane. However, the spatial dispersion from the grating did greatly affect the through-focus behavior of the excitation beam, which will be explored in more detail in section 3.2.1.

**Figure 3.4:** **Zemax excitation path simulation.** a) A simplified diagram of the excitation path and relevant optical elements was constructed to analyze the dispersion. Coverslip
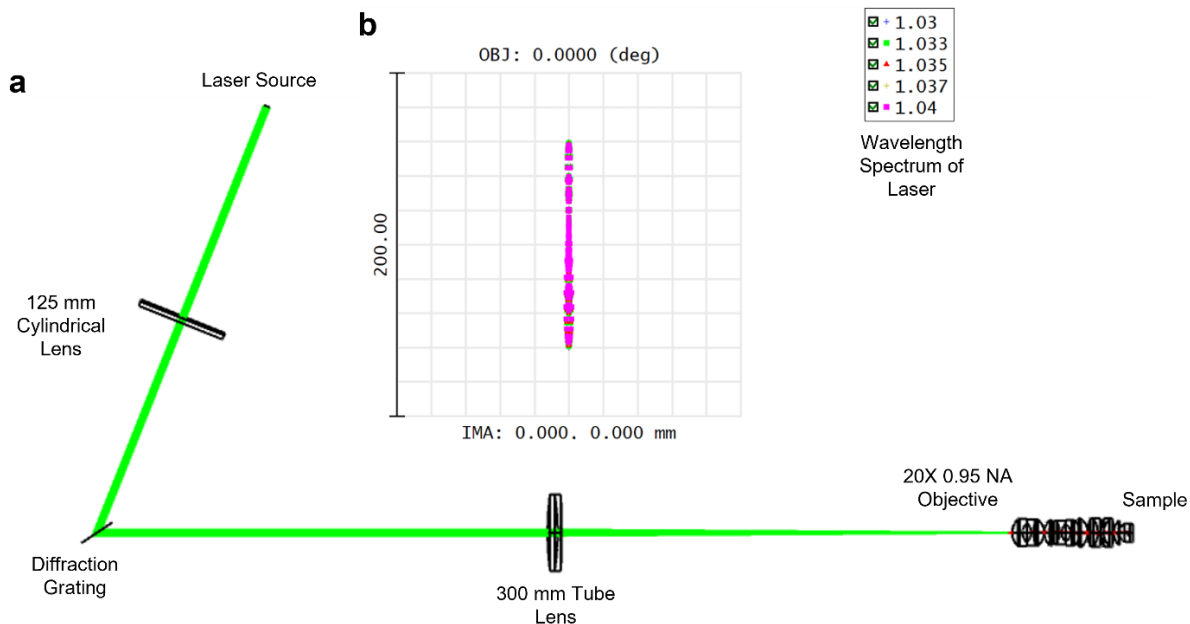


and water immersion layers were included after the objective. 5 wavelengths from 1030-1040 nm were simulated based on the linewidth of the laser. Notably the objective used has higher magnification and NA, as the 2p-LEAD objective is

custom we could not simulate it exactly. As such, all results are multiplied by 2x to better estimate the true beam sizes in 2p-LEAD. b) The simulated spot diagram of the excitation beam at the focal plane. These were used to estimate the theoretical beam and its through-focus behavior.
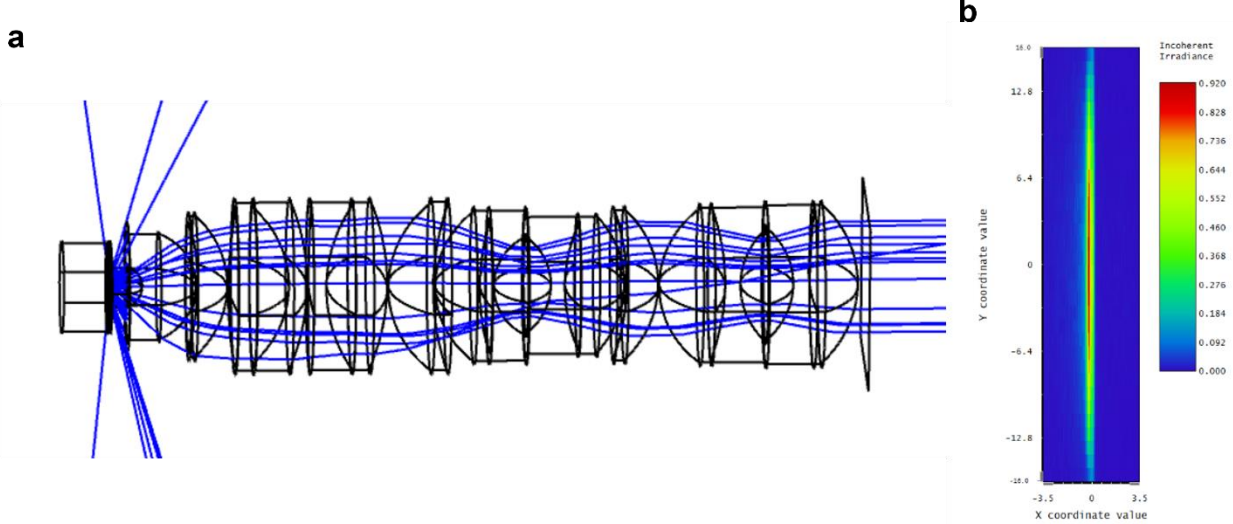
3.1.3: COLLECTION PATH MODEL

The design for 2p-LEAD is epi-fluorescent, so the emission beam is collected by the same water immersion 10x 0.6 NA objective that transmits the excitation beam. Two-photon fluorescence is dependent on the square of the incident intensity, which reduces the emission dimensions by a factor of $0.5*\sqrt{2}$, for an excited emission line of 1.8 µm x 182.0 µm ($1/e^2$ beam diameter). After the objective, the optics are designed to image this emission line to fit onto a 32 channel PMT array with a sensor area of 7 mm x 32 mm (Hamamatsu H7260 series). To minimize aberrations, an entirely separate path is constructed for the emission beam after exiting the objective back aperture. The emission beam is passed through a dichroic mirror (Thorlabs DMSP650R) which reflects near infrared light and transmits visible light below 650 nm. This mirror is place just before the objective back aperture at a 45-degree angle, which directs the excitation beam in the objective, and transmits the emission beam into a different beam path. Another 300 mm focal length tube lens is placed 300 mm from the objective back aperture, creating another intermediate imaging plane on the collection path which magnifies the beam by a factor of 16.67x. A series of lenses is included to adjust the dimensions of the emission beam to fit the PMT sensor area. Originally a 3-lens system was implemented. A 25 mm spherical lens was placed 1 focal length from the intermediate imaging plane, followed by a cylindrical lens in the y-dimension with a 300 mm focal length placed in the 4f configuration to image the intermediate imaging plane onto the PMT. These elements generate a telescope in the y-dimension that expands the beam by M = f2/f1 = 12. The telescope and objective magnification systems combine multiplicatively for a total magnification of 200 in the y-dimension, generating a 36.4 mm excitation line to fill the PMT array. In contrast, the x-dimension is allowed to diverge after the 25 mm lens until it is focused by a 75 mm cylindrical lens in the x-dimension, placed 90 mm before the PMT. This lens does not generate a magnification for the x-dimension, and merely exists to

focus the x-dimension onto the PMT array with a small spot size. Since the PMT array only includes elements in the y-dimension, the x-dimension does not need to be focused to a specific size for imaging to occur, as long as the beam is still contained in the array area.

3.1.4: COLLECTION RE-DESIGN AND FIELD OF VIEW

While the initial collection path configuration is sufficient for static imaging, we noticed that the optical elements used to focus the x-dimension negatively impacted the field of view. To simulate the collection path scanning, we implemented another model in Zemax OpticStudio in non-sequential mode, which allowed us to estimate the losses from tissue scattering as well (**Figure 3.5a**). From this model we determined that our collection efficiency is ~10% of the fluorescence intensity by comparing the detector counts with the number of rays in the ray trace. It was also noted that the scan distance is limited to 140 µm (**Figure 3.5b**). Past this point the collection beam misses the aperture of the 75 mm cylindrical lens, preventing the beam from focusing onto the PMT array. The original 75 mm cylindrical lens used was already > 2", and major optics suppliers do not carry lenses with larger apertures with 75 mm focal lengths. To improve the scan range, the optical path itself needed to be changed. The detector in our Zemax model showed that as the beam was scanned, the x-dimension of the collection beam incident on the PMT array became severely out of focus, since it was not a part of a well-characterized focus system. Thus the primary concern when re-designing the optical path was to implement a defined telescope system in the x-dimension as well.

**Figure 3.5:** **Zemax collection path simulation.** a) View of scattering simulation, with ray paths indicated in blue. Non-sequential mode was used to probabilistically estimate the emission with scattering, this is why some rays are seen missing the objective. As in the excitation path, the objective was modeled with a 20x 0.95 NA objective. Scanning experiments thus represented areas 4x what was assumed (2x for full scan width, 2x for lower magnification). b) A detector window representing the 32-channel PMT collection array. The dimensions match the PMT used in our system (7mm x 32 mm), and the incident beam size is shown in the corresponding heatmap.

To do this, 4 cylindrical lenses were used after the objective tube lens, generating 2 separate telescopes, 1 for each dimension. A range of possible lens combinations were tested by while fulfilling the following design equations:

$$f_1 + f_3 = f_2 + f_4 = 0.5 * OPL \tag{3.2}$$

$$\frac{f_4}{f_2} = M_1 \tag{3.3}$$

$$\frac{f_3}{f_1} = M_2 \tag{3.4}$$

Where $f_1$ and $f_3$ are the focal lengths of the 1$^{st}$ and 2$^{nd}$ cylindrical lenses in the y-dimension, and $f_2$ and $f_4$ are these focal lengths in the x-dimension cylindrical lenses (They are numbered based on their order in the optical path). OPL is the optical path length of the collection path after the intermediate imaging plane, $M_2$ is the y-dimension magnification, and $M_1$ is the x-dimension

magnification. Noticing that the collection efficiency was low in our simulations, we wanted to improve the collected signal by imaging a brighter section of the emitted beam onto the PMT. Thus, instead of designing our system around the full $1/e^2$ emission beam diameter, we decided to image the brighter FWHM portion of the emitted beam by increasing our y-dimension telescope magnification to 20x. Due to space constraints, the OPL was also set to an acceptable value between 400 – 600 mm. Officially the x-dimension magnification was not constrained. However, we noticed as the x-dimension magnification was reduced, the scan distance improved drastically. This is because the scanning at the sample is also magnified by the system, and images the beam to a corresponding distance from the PMT array center multiplied by the magnification in the x-dimension. The maximum scanning permitted by the system was the distance scanned before the magnified emission beam scanned off of the PMT array, which we defined as the point where only 80% of the beam remained incident on the PMT (**Figure 3.6a**). So, when minimizing the x-dimension magnification, the scan magnitude was maximized (**Figure 3.6b**).
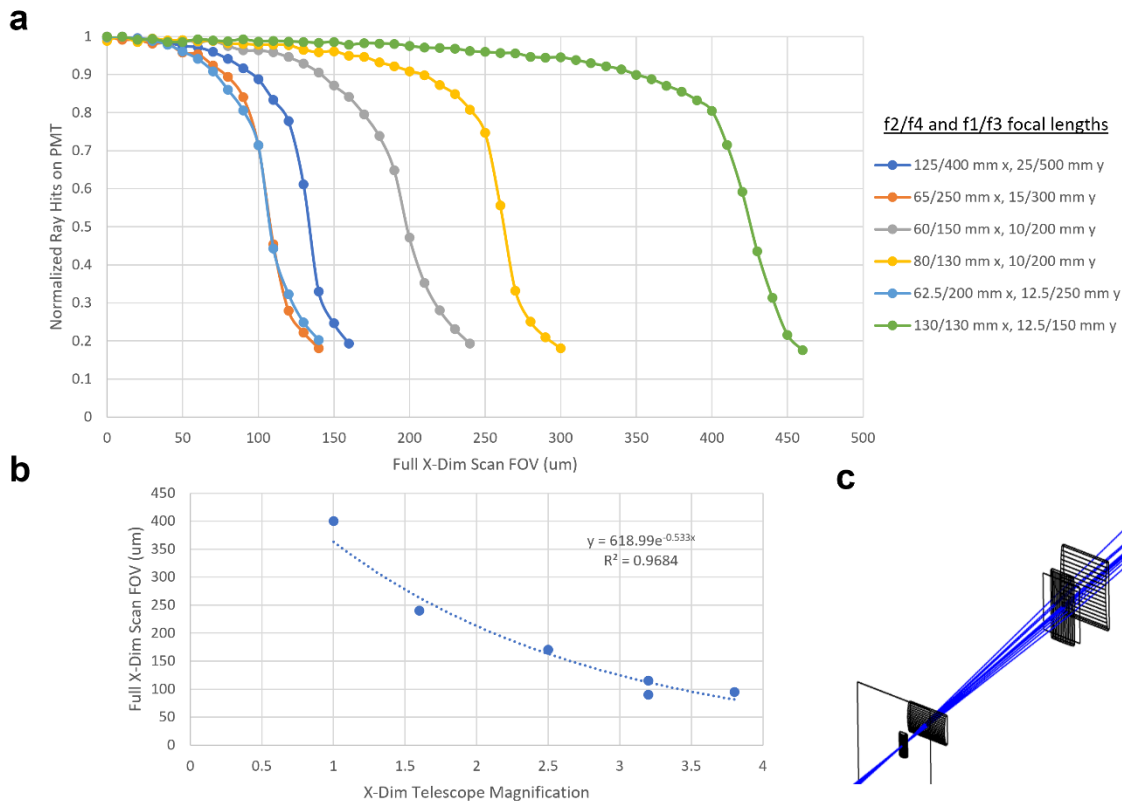
**Figure 3.6:** **Summary of FOV experiments.** a) The scanning behavior for a range of 4-lens collection path pairs. The normalized hit counts indicate what percentage of the beam is being captured by the PMT array. When this value falls below 0.8, this is considered outside the system's FOV. Lens pairs are labeled based on their order of appearance in the collection path. b) The relationship observed between the x-dimension telescope magnification in the collection path and the x-dimension scan range. It was observed that the FOV was maximized as the magnification was reduced. Blue dots represent the raw analyzed data, and the dashed line an exponential curve fit. c) Diagram of the new 4-lens collection path with optimized FOV.

Minimizing the x-dimension magnification with the other constraints produced a system with 2 130 mm cylindrical lenses in the x-dimension (M2 = 1) and a 12.5 mm cylindrical lens followed by a 250 mm cylindrical lens in the y-dimension (**Figure 3.6c**). These produce slightly different OPLs for the x and y dimension, but the difference was deemed to be negligible in our simulations due to the difference being within the Rayleigh range for the two telescope systems. Ultimately these changes broadened the scan range to 400 µm. The original collection path imaged a 160 µm line onto the PMT, which over the 140 µm scan range generated a FOV of 22,400 µm$^2$. The improved collection path shortens the portion of the line imaged onto the PMT to 96 µm, but scanning this beam over a 400 µm creates an FOV of 38,400 µm$^2$, effectively doubling the frame area while improving the collection signal.

3.1.5: SYNCHRONIZATION AND DATA ACQUISITION

The final design consideration for 2p-LEAD was the collection electronics. As previously discussed, the fluorescence signal is captured by a 32-channel linear PMT array. PMT array detection is a core component of LEAD technology, and is particularly well-suited to 2-photon microscopy, since its high gain and low noise allow it to operate in low photon-count systems. Additionally, the high > 1 GHz bandwidth allows us to detect these low photon-count signals at timescales necessary for high-speed imaging. The PMT itself is merely a collection of anodes, powered by a custom power circuit using an operation amplifier and capacitor, where the capacitor current knob is at the maximum setting (**Figure 3.7b**). An external power supply is used to provide the power for this circuit, and is generally set to 14 V for optimum gain settings without saturating

the PMT input (**Figure 3.7a**). When the PMT is covered these setting are design to generate a current output of 44 mA. To transform the PMT response into readable data, a pre-amplification circuit was design to amplify the signal (**Figure 3.8a**). A -3 dB operational amplifier is used to increase the signal by 1.4x. However, the bandwidth of the op-amp and the corresponding circuitry limits the electronic bandwidth of the system. A relatively simple circuit was constructed with a 10 pF capacitance and 5 kΩ resistance, which generates a system of 112 MHz bandwidth using the following expression:

$$f = \sqrt{\frac{GBP}{2\pi R_f C_s}} \qquad (3.5)$$

This circuit is powered by a second 2-channel external power supply. The inner cables form the ground signal and are connected to the Ground input, and the outer cables providing the ± 10 V supply are attached to the Power input via BNC connection (**Figure 3.7a,b**). The efficacy of a single channel of the pre-amp circuit was shown to have a coefficient of variance (COV) of 1.214 in a completely dark room, a reduction of 22% compared to previous design iterations (**Figure 3.8b**).

**a**
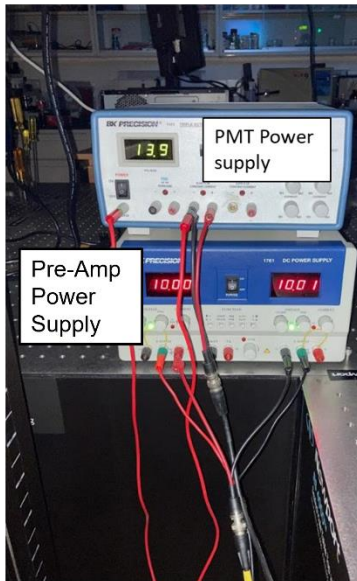


**b**
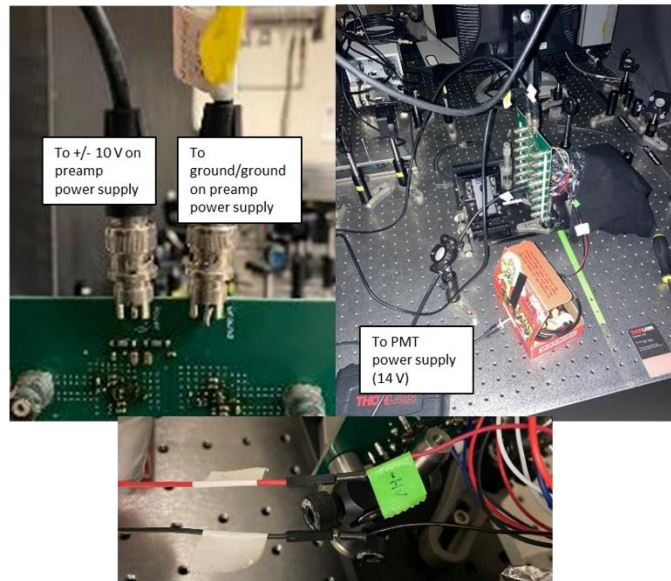
**Figure 3.7:    PMT and pre-amp power circuitry.** a) The power supply configuration for the PMT (top power supply) and pre-amplification board (bottom power supply). b) The power supply connections for the pre-amp and PMT. The top left shows the cable orientation into the pre-amp. In this case, the outer cable pair in a) corresponds to the ground/ground connection, and the inner cables to the $\pm$ 10 V. In addition, the PMT power supply is fed to a custom power circuit (upper right) and then connected through pin cables to the PMT directly (bottom image).



a

b
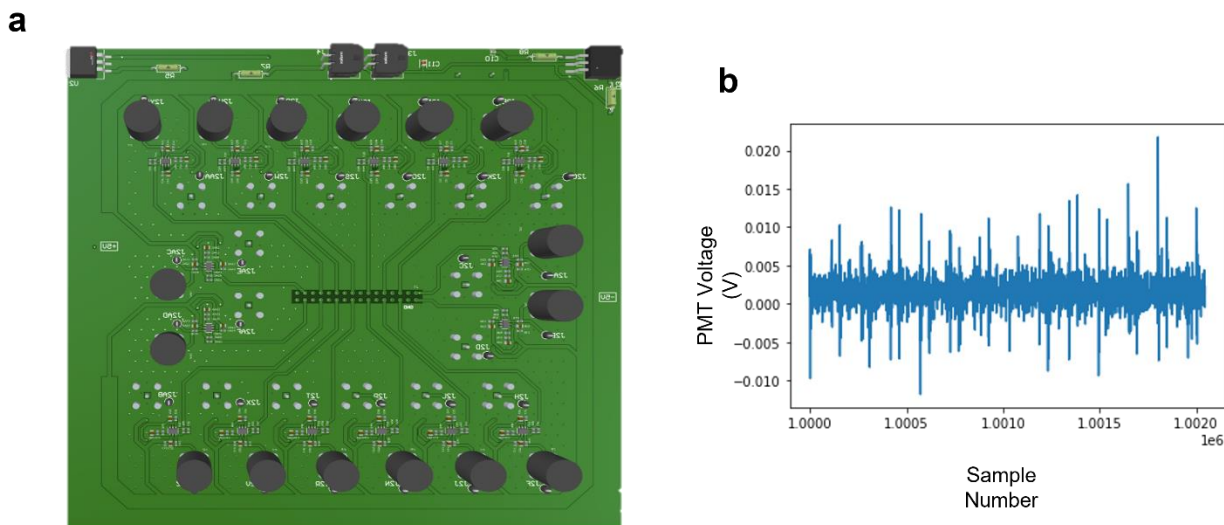
**Figure 3.8:    Pre-amplification circuit design and characterization.** a) Shows the updated pre-amplification circuit with its corresponding elements on a PCB board. b) Shows the various in registered PMT voltage in a dark room. The covariance of this data was taken as a way to characterize the electronic noise of the system.

The output from the pre-amp circuits are read by a data-acquisition card that is synced with both the laser output and galvo scanning mirror. The 16-channel DAQ (AlazarTech ATS9416) is able to read up to 100 MSa/s from each channel using the DAQs internal clock, which we initially used. However, this leaves 10 ns resting time between samples, and the fluorescence emission peak is on the order of 1-5 ns. In addition, the laser output pulses, though consistent, are generally frequencies not divisible by the sample time, such as 9.8 MHz. As such, we noticed that the fluorescence signal and data acquisition would frequently come in and out of sync when using the DAQ internal clock. We then switched to using the 2.5 V TTL signal from the laser sync1 output as an external clock for the DAQ for direct pulse-to-pulse synchronization (**Figure 3.9a**). The TTL signal is first delayed with a co-axial cable box (Stanford Research Systems DB64) to correspond

to the fluorescence peak on the PMT, by manually adjusting the delay until maximum signal was observed at 17.5 ns delay (**Figure 3.9b**). After the delay the signal is reduced with a 10 dB attenuator to meet the 0.250 V < V_in < 2.2 V input voltage requirement to the DAQ ECLK SMA connection. Implementing this syncing between the fluorescence emission and data acquisition generated much more consistent data and improved our collection signal by 3x by sampling closer to the actual fluorescence peak (**Figure 3.9c**). Finally, syncing was also created between the data acquisition and galvomirror by sacrificing one of the DAQ inputs. Instead of receiving information from the PMT, the 16th channel of the DAQ receives a sync-out signal from the function generator which controls the galvomirror. Each rising edge of the triangle waveform generates an impulse signal as it crosses zero. Tracking the impulse signals with the DAQ and then adjusting for the fixed delay between the function generator input at mirror response enables the scan location to be estimated as assigned to the incoming data.



43
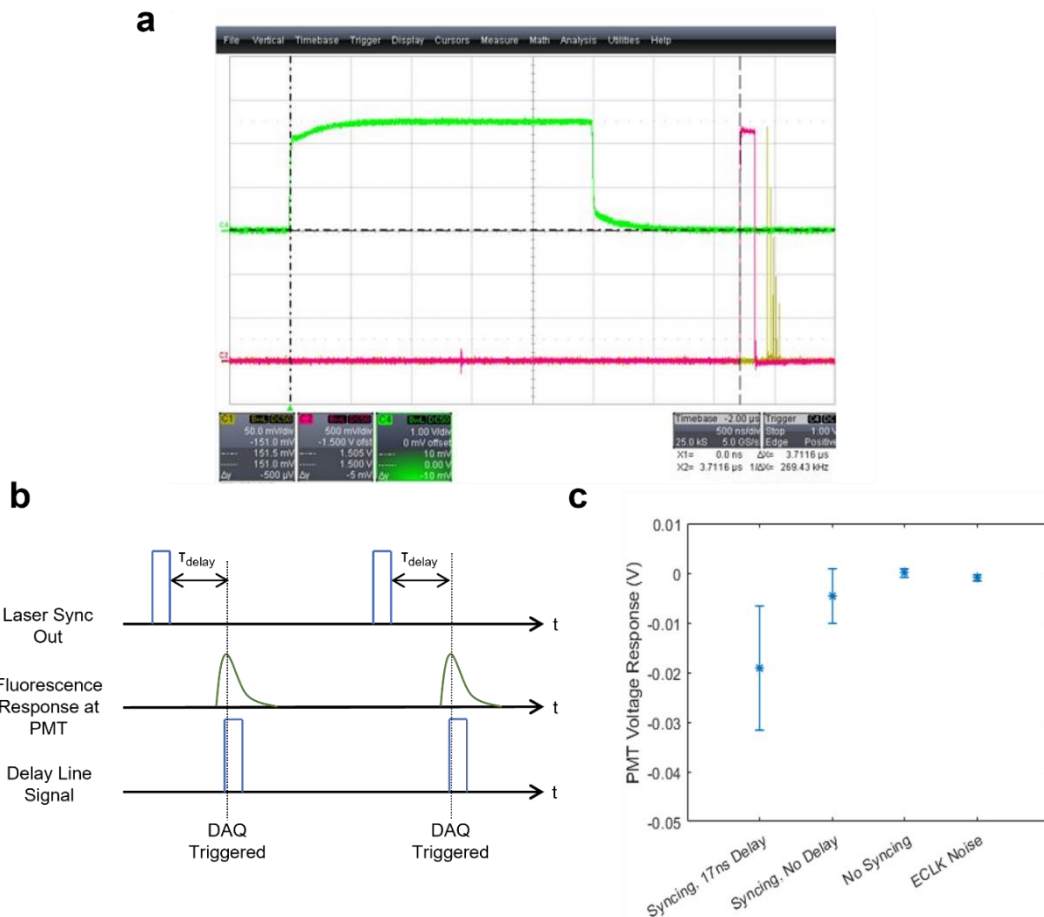
**Figure 3.9:** **Pulse syncing analysis.** a) Characterization of the laser synchronization signal. Divisions are 500 ns along the x axis and 500 mV along the y axis. The pink line corresponds to the synchronization signal, and the yellow line to the laser output. The separation between the two indicates there is a small delay between these two events, but this delay was observed to be consistent and characterizable. b) A simplified diagram of the synchronization process. The sync signal from the laser is delayed by a fixed amount such that the rising edge of the TTL matches the peak fluorescence response incident on the PMT. c) Comparison of the average and standard deviation of the PMT voltage with a 5 mM rhodamine sample with < 100 mW at the sample and 10 MHz laser repetition rate. Data collected with the external clock controlled by the laser synchronization signal exhibited a 3x increase in signal. A sharp increase in the standard deviation was also observed. This is due to the presence of "dropouts" in the data. They are present in all samples, but their presence becomes a further deviation from the signal as the signal increases, thus biasing the signal standard deviation.

3.1.6: SCATTERING

A common design issue with high-power ultrafast systems is mitigation of scattering. Even with highly efficient elements, when using such high powers even a small percentage of uncontrolled light can generate significant scattering. This is of particular concern in our system, as the PMT is sensitive enough to detect single photon counts. Though the PMT's cathode ray sensitivity is < 0.1% at our excitation wavelength, we noticed a high level of noise which scaled linearly with an increase of the excitation power, indicating scattered light from the excitation beam was entering the detector and skewing the data (**Figure 3.10**). This issue was amplified once we integrated the transmission diffraction grating, so we hypothesized this element may contribute significantly. Approximately 6% of the light passing through the grating is directed into other diffractive orders, even at its most efficient orientation, so beam traps (Thorlabs BT610) are placed at the 0 and +1 reflected orders to extinguish scattering from these orders. Similarly, a beam trap was placed below the sample plane to prevent scattering from the excitation beam on the bottom of the enclosure. The excitation and emission paths were also moved to different heights to make excitation scattering less likely to reach the detector. Finally, a laser-safe absorbing cover was placed around the PMT and its cables, and preliminary housing was designed to isolate the PMT and associated electronics from the rest of the system. Implementing these improvements reduced

44

scattering by 6.57x, allowing 2p-LEAD to operate at high-powers and resolve signal from the scattering background noise.
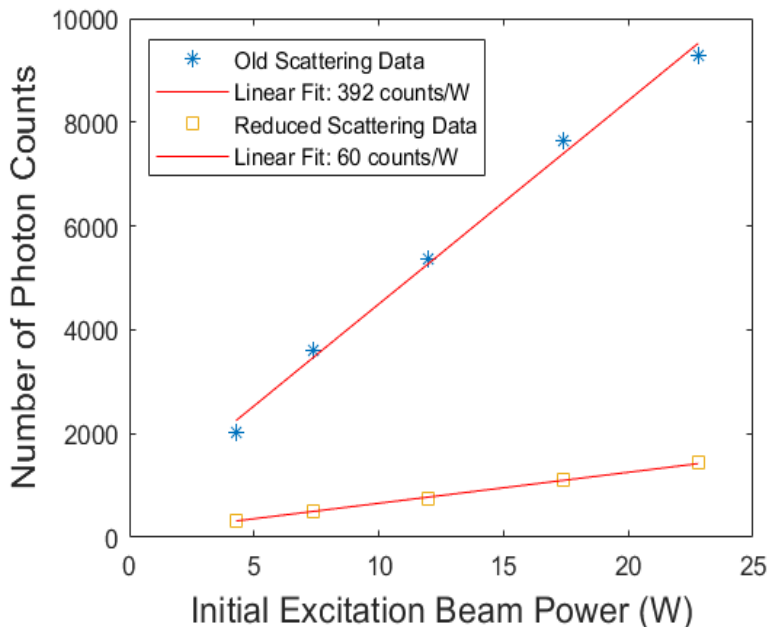


**Figure 3.10:** **Scattering behavior comparison.** Plot shows the measured photon counts across channel 9 over a range of initial excitation beam laser powers. The first set of data was acquired from the initial system, and the second set from the system after implementing the various scattering mitigation strategies. In both cases, the scattering scales linearly with excitation power. The slope of the linear fits were used to estimate the scattering reduction.

## 3.2: MICROSCOPE CHARACTERIZATION

### 3.2.1: BEAM PROFILING

The first step of design verification included profiling different locations along the beam path using an addition to the typical 2p-LEAD setup. A new set of conjugate planes was constructed below the objective lens, consisting of a second 20x 0.95 NA water immersion objective followed by a 50 mm tube lens (**Figure 3.11a**). The initial spacing between the two objectives was equal to the sum of their working distances, so the focused excitation beam was imaged directly by the second objective. As both objectives required water immersion, a thin 170 μm glass slide was placed between the objectives and water was dripped above and below to

45

effectively cover both objective lenses. To prevent aberrations induced by imaging the slide, care was taken to ensure the excitation line was focused to a plane above or below the glass slide. After objective preparation, a 50 mm tube lens was placed one focal length from the back aperture of the second objective in a tube mount, and the beam profiler was placed one focal length below the 50 mm tube lens. This configuration creates a conjugate plane between the plane imaged by the second objective and the beam profiler with a 5.56x magnification of the beam onto the beam profiler. A micrometer stage with 10 µm ticks was used to translate the second objective and tube lens, allowing different portions of the excitation signal away from the focus to be imaged by the beam profiler. For each profile, a gaussian fit was taken of the data to estimate the $1/e^2$ beam diameter:

$$f(x) = Ae^{-0.5\left(\frac{x-x_0}{\sigma_x}\right)^2} \tag{3.6}$$

Where $x = 2\sigma_x + x_0$ is the location of the $1/e^2$ beam radius. From these data, a through-focus profile of the excitation beam behavior was constructed comparing the beam diameters at different distances from the focal plane. These results were fit to the gaussian beam propagation equation to characterize the tightness of their focus, and better estimate the true focal plane beam size:

$$w(z) = w_0 + \sqrt{1 + \left(\frac{z}{z_R}\right)^2} \tag{3.6}$$

Where $w_0$ is the beam waist ($1/e^2$ beam radius), $z$ is the distance from the focal plan along the optical axis, and $z_R$ is the Rayleigh range. The Rayleigh range is the point at which the beam expands to $\sqrt{2}*w_0$, and in this region the beam remains roughly collimated.
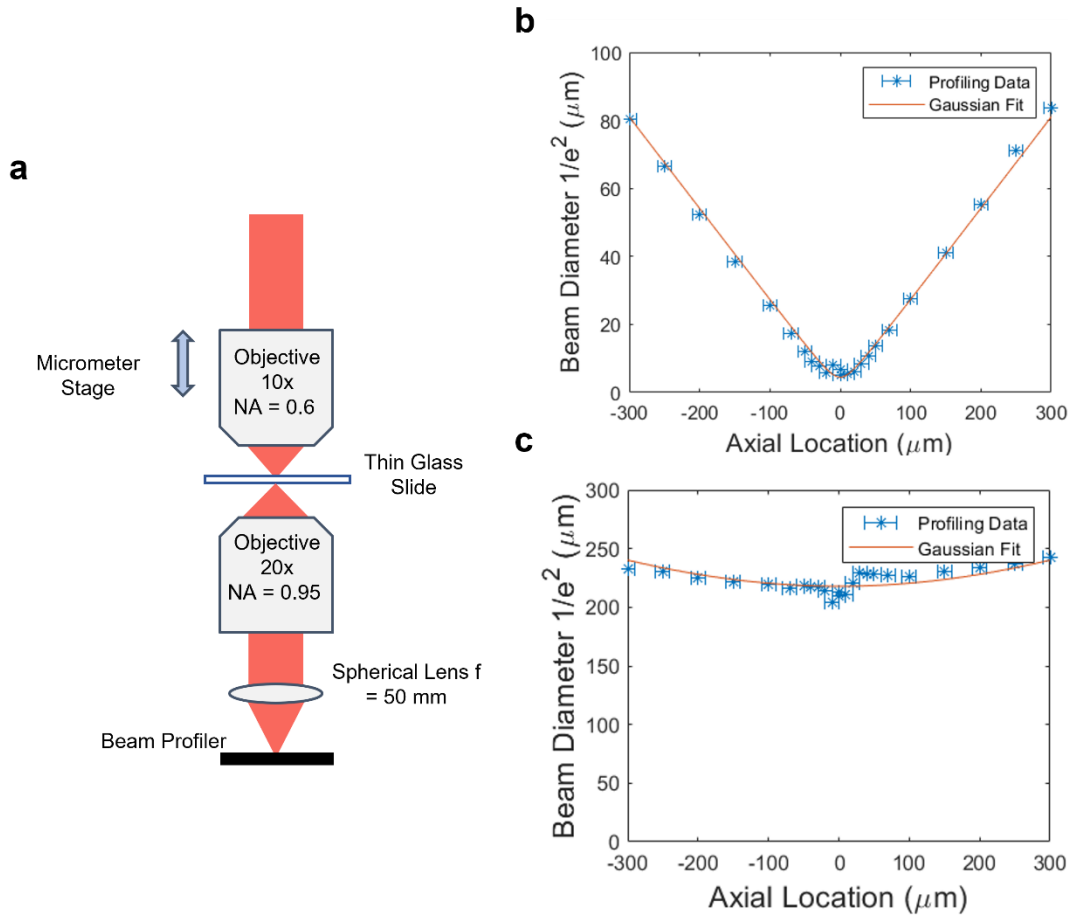
**Figure 3.11: Beam profile experiments.** a) The experimental setup for beam profiling near the sample focal plane. A second 20x 0.95 NA objective and 50 mm tube lens pair image the excitation beam onto a beam profiler. A micrometer stage translates the 10x objective so different portions of the excitation beam are imaged. b) The through-focus beam profile in the x-dimension with temporal focusing. Individual data points are shown in blue, and the best gaussian fit is shown in red. Strong focusing was observed, as expected by our theoretical model. c) Through-focus beam profile in the y-dimension with temporal focusing. This dimension has much weaker focusing behavior. Without spatial dispersion from the diffraction grating the beam diameter is constant instead. All points have $\pm 0.3$ µm uncertainty in the x and y dimensions due to the de-magnified detector pixel pitch, and $\pm 5$ µm uncertainty in the z-dimension due to the tick resolution of the micrometer stage.

Applying these fits, we found that at the focal plane, with temporal focusing, the estimated $1/e^2$ beam diameter was $4.5 \pm 1.5$ µm in the x-dimension, and $222.6 \pm 9.6$ µm in the y-dimension (**Figure 3.11b,c**). The proportionally large error present in measurements of the x-dimension arises from the low magnification of the experimental setup. Each element of the beam profiler is 3.69 µm. With 5.56x magnification of the theoretical beam, we would expect a 13.3 µm $1/e^2$ diameter

beam in the x-dimension incident on the beam profiler. At the focus, this allows < 5 pixels to image the full beam diameter, leading to large uncertainty in the exact beam profile when imaging close to the focus. Unfortunately, the available space below the first objective is limited (~20mm), which prevents the use of larger focal length tube lenses that could increase the magnification. Despite this, the theoretical value for the x-dimension $1/e^2$ beam diameter at the sample plane of 2.4 µm is not far beyond the uncertainty of the beam profile measurements. In the y-dimension, we have consistently noticed profiles measuring a shorter linewidth than expected, which may be caused by issues focusing the y-dimension of the beam exactly on the back aperture of the objective. Strong focusing behavior was observed in the x-dimension as predicted, and very slight focusing was observed in the y-dimension. Without the diffraction grating, the y-dimension beam is designed to be collimated exiting the objective. Since temporal focusing introduces spatial dispersion as well, it was expected that this would introduce some focusing in the y-dimension, since the spatial dispersion prevents the y-dimension beam from being fully focused on the objective back aperture. Overall, the experimental results are in rough agreement with our theoretical predictions.

The beam profiler was also used to calibrate the scanning field of view between the galvomirror and function generator. The frequency of the galvomirror oscillation was set to 500 Hz and 1,500 Hz with either a triangle or sinusoidal waveform input. For each of these four frequency settings, a range of voltages were applied from 0.1-0.8 V (**Figure 3.12a**). These scans were collected by the beam profiler, which registered the dwell time of the scanned beam as intensity (**3.12b,c**). Using this visual representation of the dwell time, an estimated scan range could be calculated, in addition to the relative speed of the galvomirror throughout the scan cycle. Analyzing these data showed an exactly linear relationship between input voltage amplitude and scan range that was numerically characterized by a linear equation. These results also demonstrated the sinusoidal signal exhibits a much greater variation in scan speed than triangle waveforms. Variations are undesirable, since they cause non-uniformity in the image scale that

needs to be calibrated. Thus these experiments provided justification to use triangle wave inputs in addition to aiding in electronic calibration.
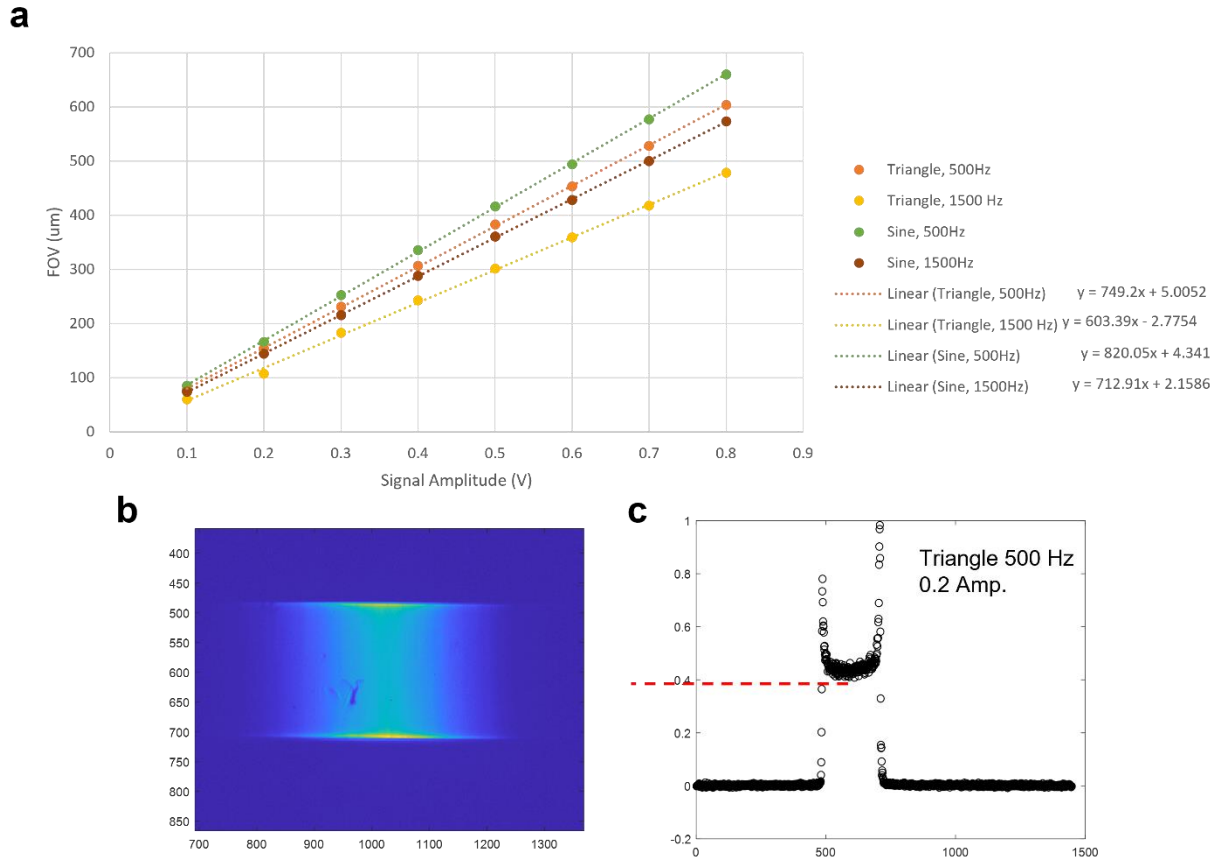


**Figure 3.12:** **Scan range calibration with beam profiler.** a) Summary of scan range trials for different input signal shapes and amplitudes. Results were exactly linear and could be characterized by equations. These calibration curves served as a basis for scan range estimation, and when we used values outside those given we estimated the scan range through linear interpolation. b) A sample scan incident on the beam profiler with 0.2 V 500 Hz triangle wave signal. c) Sample intensity cross section along the scan dimension registered by the beam profiler. Higher intensity corresponds to higher dwell time, which occurs when the galvomirror scans the beam more slowly over a particular region. Dwell time was largest at the edges, since the galvomirror has to slow switch scan directions.

## 3.2.2: PULSE WIDTH WITH TEMPORAL FOCUSING

Characterizing the pulse width throughout the system required a custom Michelson interferometer (**Figure 3.13a**). The PulseCheck autocorrelator could not be used for

49

autocorrelation measurements within the system itself, since the PulseCheck requires the incoming light to be <collimated and aligned with a very specific polarization, which logistically was not feasible to implement elsewhere in the system. Instead, we used a 50/50 beam splitter and two mirrors set on translation stages before the primary 2p-LEAD optics. The position of the mirrors was adjusted so the split beams recombined and interfered before entering 2p-LEAD. The interference pattern generates fringes in the excitation beam, which in turn generates fringes in the fluorescence emission. A thin slide of rhodamine 6G was used as a fluorescent dye and captured by the PMT. The observed fringes created exhibit a magnitude 8x the base emission signal level at their peak due to the combination of two beams constructively interfering (2x signal), and the emission having an $I^2$ dependence on the excitation bean (4x signal) (**Figure 3.13b**). Additionally, areas of destructive interference can be observed in the signal dips observed in the fringe region near the center of the pulse width. For analysis, one channel of these results was read, a gaussian fit was applied to the autocorrelation fringe pattern, and the results were deconvolved to obtain the estimated pulse width FWHM. As with the beam profile, the through focus pulse width was determined by adjusting the objective on a micrometer stage with a 10 µm resolution. This causes the excitation beam at different distances from the focus to excite the rhodamine instead of the focused section. Because of this, the uncertainty in the system will result directly from the slide thickness used. Close to the focus, sample thicknesses of 7.7 µm were used, so the primary source of uncertainty was from the stage resolution. However, farther from the focus samples of up to 46 µm thickness were used to increase the signal intensity, increasing the uncertainty to ± 23 µm.
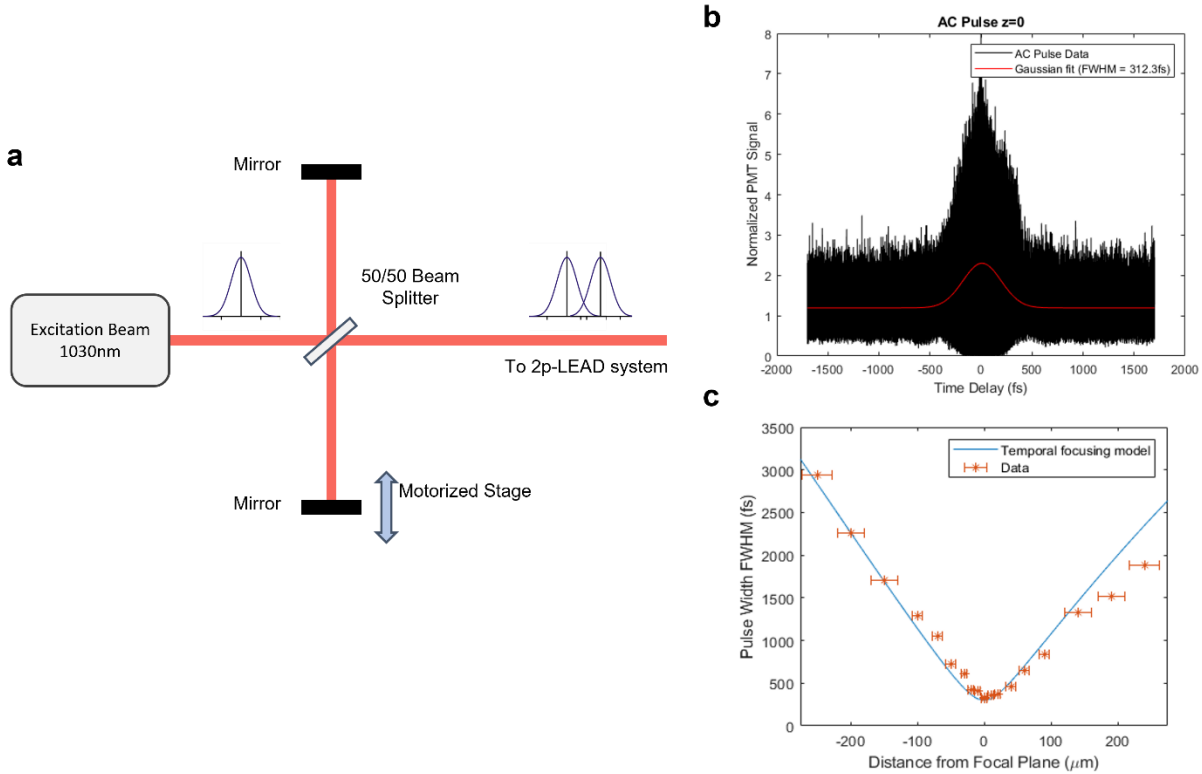
**Figure 3.13: Temporal focusing experimental results.** a) Diagram of Michelson interferometer before the main 2p-LEAD optics. Pulses are interfered with a 50-50 beam splitter and two mirrors. b) Sample autocorrelation pulse obtained with fluorescence emission from a single channel of the PMT array. Red line indicates illustrates the gaussian fit to the pulse width, and the black is the sampled data, with a range of 8x the signal base. c) Pulse width FWHM data for various distances from the focal plane, fit to the expected temporal focusing behavior. Uncertainties are determined by the slide thickness needed to obtain sufficient signal for imaging.

A through-focus profile of the pulse width FWHM with temporal focusing was constructed, and fit results estimate a focus pulse width FWHM of 492 fs (**Figure 3.13c**). This central value for the autocorrelation is higher than expected, and may arise from difficulty locating the true focal plane with the ± 5 µm uncertainty of the micrometer stage. Earlier results using the custom 2p-LEAD interferometer without temporal focusing implemented generated a measured pulse width of 312 fs, which also matches the pulse width values exiting the laser before the LEAD setup explored in section 3.1.1. Away from the focus, we also notice that the results closely match the experimental predictions based on the system parameters. Using the mathematical relationships outline in section 2.2.2 (**Eqns. 2.2 and 2.3**) we set f = 0.003 m (working distance of the objective),

k = 6.07*10$^6$ m (wavenumber for a 1035 nm beam), Ω = 7.85*10$^{12}$ Hz (Temporal FWHM bandwidth expected assuming a 300 fs pulse), s = 5.4*10$^{-5}$ m (Based on beam FWHM in y-dimension at the objective back aperture at objective back aperture without dispersion), α = 2.5*10$^{-16}$ m/Hz (scaling). These experiments verify that our system properly implements temporal focusing, and the excitation pulse width broadens away from the focus.

## 3.2.3: BEAD IMAGING AND RESOLUTION

2 µm diameter polystyrene beads were imaged to characterize the system resolution based on the procedure outlined in background section 2.3.5. First the bead samples were prepared through a series of dilutions. The first dilution was made in water, and after the dilution the beads were  bath sonicated for >2 hours to prevent the beads from self-adherence. During this sonication process 2% agar was heated to its melting point. Once the bead and water solution was properly sonicated, a final dilution was made by pipetting the bead solution into the agar, and then spinning the agar solution to encourage the beads to disperse within the sample. Finally, a 5-10 µm sample is pipetted onto a thick microscope slide. A solid sample is used to ensure the beads were not moved by our water immersion objective. The thickness of the sample is controlled by using tape "buffers" of known thickness and placing a 18 mm x 18 mm coverslip atop the tapes. This fixes the distance between the top of the microscope slide and the coverslip to a known distance, fixing in turn the sample thickness. For resolution experiments, thin samples of ~50 µm thickness were used, to prevent scattering from interfering with our results.

A specific procedure was developed to ensure imaging took place within the sample volume. Before imaging the sample, a thin slide of rhodamine was scanned with the same range and frequency as the desired scanning for the beads. Obtaining these data allowed us to calibrate the number of samples per frame, and compare the frame placement to the impulse timing data to characterize the offset between the two (**Figure 3.14b**). This way, we could know our location in the imaging frame, even with a mostly dark frame like what is obtained during bead imaging. After the frame is characterized, a second procedure is performed for proper axial sample placement.

The top of the sample slide and bottom of the coverslip are marked with ink at different portions of the sample. The marked slide is then placed below the 2p-LEAD objective and immersion media placed between the slide and objective as well. We then take advantage of the intermediate imaging plane in the collection path, and use a flip mirror to re-direct the path to a visible CCD camera placed at the new intermediate imaging plane location. A collimated light source is placed below the sample, which in this new configuration images the sample to the CCD with a brightfield background (**Figure 3.13a**). A micrometer stage with 10 µm ticks is used to translate the sample until each of the two marking comes into focus. These focus positions provide the borders of the sample, allowing us to determine a more exact estimate of the sample thickness and ensure our system images within the sample volume. Once the placement is determined, imaging could occur.
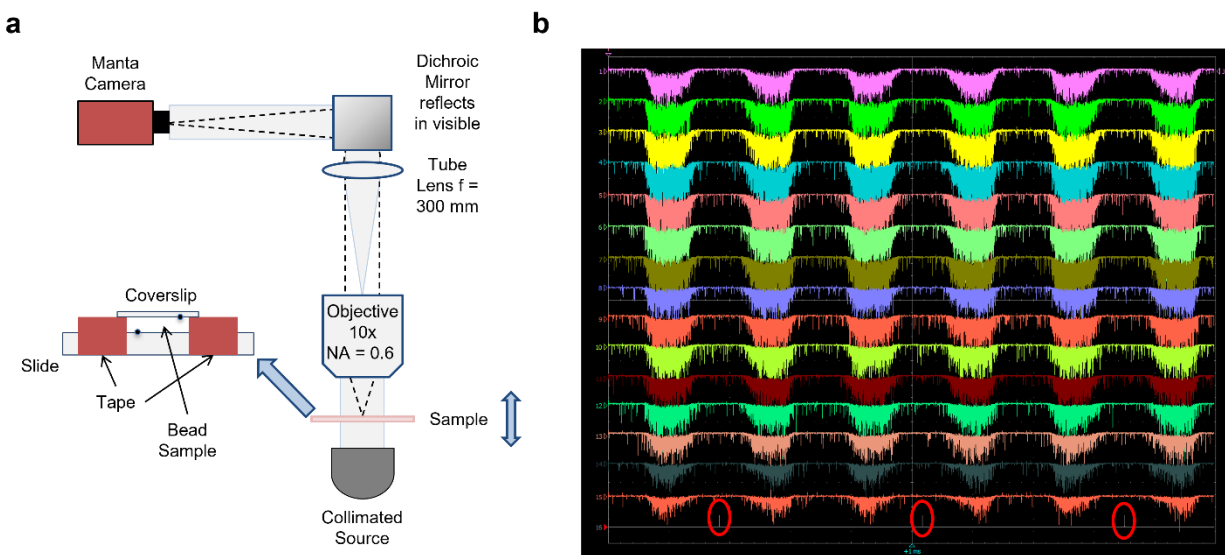


**Figure 3.14:** **Bead sample calibration.** a) Diagram of the optical setup to properly position the bead sample to ensure the focal plane is within the sample volume. The arrow on the left points to a diagram of the sample slide, with the two dots representing the markings on the slide to determine the sample top and bottom. The camera is placed at the intermediate imaging plane of the system, so when the sample is positioned correctly it will focus onto the camera detector. b) A screenshot of the DAQ system oscilloscope view when scanning rhodamine with a 0.4 V 1.5 kHz triangle wave input to the galvomirror. Areas of signal drop indicate the rhodamine scan is being properly imaged by the PMT, and dead areas indicate the galvomirror is scanning beyond the range of what the PMT can collect. The red circles on the 16th channel correspond to the impulse synchronization signal from the function generator controlling the galvomirror. These data are compared with the data in the rhodamine channels to identify the image frame and offset.

53

Bead images were successfully obtained at 3,000 fps, with the line scanned across a 238.6 µm range and collected by a 16-channel PMT array with a 16 mm length. Since only 16 mm of the 36.4 mm emission line is imaged by the PMT, and only 15 channels were used for imaging (one channel is devoted to clocking the galvomirror position) this reduced the y-dimension of the emission line in the frame to 75 µm. In addition, a scan range beyond the possible FOV for the system was chosen to ensure the scanning speed over the frame was uniform, and to limit the number of pulses per bead to avoid damage. Ultimately these conditions generated a 170 µm x 75 µm FOV with an SBR ~13 over a single frame (**Figure 3.15**). Areas of lower signal intensity correspond to out of focus beads, whereas beads in focus will display higher signal and larger widths. In this sample, many of the beads are clustered together, since the beads were not properly dispersed in the agar sample during dilution. Nonetheless, beads are still distinguishable.
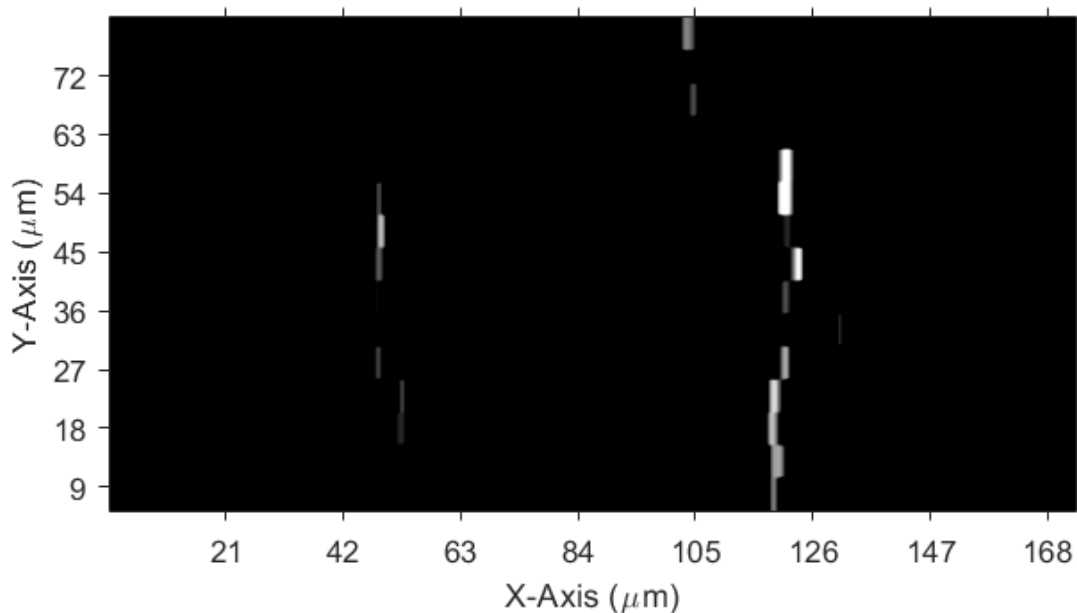


**Figure 3.15: 5 frame averaged 2 µm bead image.** The resulting image of 2 µm diameter polystyrene beads suspended in agar solution across a 170 µm x 75 µm frame. The image is a frame average of 5 consecutive frames. Bright areas correspond to the presence of beads, and black indicates the background. Areas of darker signal indicate out of focus beads.

# Chapter 4: Conclusions and Future Work

This thesis outlined the background, design, construction, and characterization of a two-photon line excitation and array detection system. The resulting microscope was able to successfully image 2 µm diameter beads across a 170 µm x 75 µm FOV at 3,000 fps with a 10 MHz laser repetition and sampling rate at 450 mW power. The system's spatial and temporal focusing characteristics matched experimental predictions based on the original optical design and Zemax simulations. A single frame 2 µm bead image had an SBR ~13, with the signal easily distinguishable over the electronic noise and background scattering. Improvements were made to the system to increase the FOV for future imaging endeavors to 400 µm x 96 µm.

The base design explored in this thesis provides a proof of concept for further extensions on 2p-LEAD technology. Future iterations of this design will utilize an AOD as the primary in-plane scanning mechanism, enabling the microscope to operate at >50 MHz frame rates. Based on the powers used in our experimentation at 10 MHz, the power increase needed with increased sampling would normally cause thermal damage in a point scanning system (>250 mW) [48]. However, we anticipate we may be able to avoid this damage due to the long excitation line reducing the fluence at the sample. Simulations performed by other lab members have indicated ~600 mW excitation may be the upper threshold without active cooling, but further investigation and tissue heating experiments are needed to confirm this hypothesis and clear the system for functional *in vivo* imaging.

Several other aspects of the system will require adjustments moving forward. In point-scanning systems with wavelengths similar to 2p-LEAD, the imaging become scattering limited ~ 400 µm in mouse brain samples [49]. Since line-scanning is much more susceptible to scattering, there is reason to believe these depth limits may be significantly lower for 2p-LEAD. To further reduce the potential effects of scattered light entering the detection system and reducing the imaging depth, a full enclosure should be built around the microscope collection path. This may prove challenging with the large rectangular lenses used in the collection path, requiring custom

mounts to properly enclose, but this change will be important to allow the microscope to detect weaker fluorescence features in samples, and ultimately image deeper *in vivo*. These imaging depth experiments will also require an axial scanner, likely an ETL, that can image >100 µm range at repetition rates >500 Hz to achieve the 1,000 VPS goal of 2p-LEAD imaging. Before implementing any design changes, immediate next steps include image-depth characterization using scattering phantoms, verifying tissue heating properties, and functional imaging. Despite the challenges in initial design, the system limitations, and future work, 2p-LEAD has shown to be a promising technology for future in vivo neural imaging efforts. Continuing to improve microscope imaging speeds advances the experimental possibilities in neuroscience and other areas of biology, ultimately benefiting the discipline and modern medicine and healthcare.

# References

1.  K. Thorn, "A quick guide to light microscopy in cell biology," *Mol. Bio Cell*. **27**(2): 219-222 (2016).
2.  J. G. Fujimoto, C. Pitris, S. A. Boppart, and M. E. Brezinski, "Optical Coherence Tomography: An emerging technology for biomedical imaging and optical biopsy," *Neoplasia*. **2**(1-2): 9-25 (2000).
3.  H. J. Butler, et. al., "Using Raman spectroscopy to characterize biological materials," *Nat. Protoc*. **11**(4): 664-687 (2016).
4.  M. J. Sanderson, I. Smith, I. Parker, and M. D. Bootman, "Fluorescence Microscopy," *Cold Spring Harb. Protoc*. **2014**(10): 1042-1075 (2014).
5.  R. Datta, T. M. Heaster, J. T. Sharick, A. A. Gillette, and M. C. Skala, "Fluorescence lifetime imaging microscopy: fundamentals and advancements in instrumentation, analysis, and application," *J. Biomed. Opt*. **25**(7): 1-43 (2020).
6.  W. R. Zipfel, R. M. Williams, and W. W. Webb, "Nonlinear magic: multiphoton microscopy in the biosciences," *Nat. Biotechnol.* **21**(11): 1369-1377 (2003).
7.  M. Z. Lin, and M. J. Schnitzer, "Genetically encoded indicators of neuronal activity," *Nat. Neurosci.* **19**(9): 1142-1153 (2016).
8.  G. M. Shepherd, "The microcircuit applied to cortical evolution: from three-layer to six-layer cortex," *Front. Neuroanat.* **5**: 30 (2011).
9.  Y. Bando, C. Grimm, V. H. Cornejo, R. Yuste, "Genetic voltage indicators," *BMC Biology,* **17**(1): 71 (2019).
10. P. W. Winter, and H. Shroff, "Faster fluorescence microscopy: advances in high speed biological imaging," *Curr. Opin. Chem. Biol.* **20C**(1): 46-53 (2014).
11. C. Boudoux, "Fundamentals of Biomedical Optics," *Pollux* (2017).
12. M. Göppert-Mayer, "Uber Elementarakte mit zwei Quantensprungen", *Ann. Phys.* (Paris) 9, 273 (1931).
13. W. Denk, J. H. Strickler, and W. W. Webb, "Two-Photon Laser Scanning Fluorescence Microscopy," *Science.* **248**(4951): 73-76 (1990).
14. P. T. C. So, C. Y. Dong, B. R. Masters, and K. M. Berland, "Two-Photon Excitation Fluorescence Microscopy," *Annu. Rev. Biomed. Eng.* **2**: 399-429 (2000).
15. G. Zhu, J. van Howe, M. Durst, W. Zipfel, and C. Xu, "Simultaneous spatial and temporal focusing of femtosecond pulses," *Opt. Express.* **13**(6): 2153-2159 (2005).
16. E. Papagiakoumou, E. Ronzitti, and V. Emiliani, "Scanless two-photon excitation with temporal focusing," *Nat. Methods.* **17**(6): 571-581 (2020).
17. A. Vogel, J. Noack, G. Hüttman, and G. Paltauf, "Mechanisms of femtosecond laser nanosurgery of cells and tissues," *Appl. Phys. B.* **81**(8): 1054-1047 (2005).
18. J. L. Boulnois, "Photophysical processes in recent laser developments: A review," *J. Lasers Med. Sci.* **1**(1): 47-66 (1986).
19. A. Bullen, S. S. Patel, and P. Saggau, "High-Speed, Random-Access Fluorescence Microscopy: I. High-Resolution Optical Recording with Voltage-Sensitive Dyes and Ion Indicators," *Biophys. J.* **73**(1): 477-491 (1997).
20. W. Akemann, et. al., "Fast optical recording of neuronal activity by three-dimensional custom-access serial holography," *Nat. Methods.* **19**(1): 100-110 (2021).
21. G. Katona, et. al., "Fast two-photon *in vivo* imaging with three-dimensional random-access scanning in large tissue volumes," *Nat. Methods.* **9**(2): 201-208 (2012).

22. G. R. B. E. Römer, and P. Bechtold, "Electro-optic and Acousto-optic Laser Beam Scanners," *Phys. Procedia.* **56**: 29-39 (2014).
23. L. Chen, M. Ghilardi, J. J. C. Busfield, and F. Carpi, "Electrically Tunable Lenses: A Review," *Front Robot AI.* **8** (2021).
24. M. Duocastella, et. al., "Acousto-optic systems for advanced microscopy," *J. Phys. Photonics.* **3** (2021).
25. W. C. Wang, "Optical Detectors," *Nat. Tsing Hua University.*
26. D. J. Kissick, R. D. Muir, and G. J. Simpson, "Statistical treatment of photon/electon counting; extending the linear dynamic range from the dark count rate to saturation," *Anal. Chem.* **82**(24): 10129-10134 (2010).
27. "High Speed Detector Terminology," *MKS Newport* (2023).
28. B. Tabbert, and A. Goushcha, "Optical Detectors," Springer Handbook of Optics and Lasers, *Springer* (2012).
29. R. Hui, "Introduction to Fiber-Optic Communications," *Academic Press* (2019).
30. V. A. Magnotta, and L. Friedman, "Measurement of Signal-to-Noise and Contrast-to-Noise in the fBIRN Multicenter Imaging Study," *J. Digit. Imaging.* **19**(2): 140-147 (2006).
31. G. Holst, "Scientific CMOS Camera Technology: A breeding ground for new microscopy techniques," *Microscopy and Analysis* (2014).
32. "Si photodiodes," *Hamamatsu Photonics K. K.* (2022).
33. "Photomuliplier Tubes: Basics and Applications," *Hamamatsu Photonics K. K.* (2007).
34. K. Becker, et. al., "Deconvolution of light sheet microscopy recordings," *Sci. Rep.* **9**(17625): (2019).
35. E. L. Dereniak, and T. D. Dereniak, "Geometrical and Trigonometric Optics," *Cambridge: Cambridge University Press* (2008).
36. J. Antonello, D. Burke, and M. J. Booth, "Aberrations in stimulated emission depletion (STED) microscopy," *Opt. Commun.* **404**: 203-209 (2017).
37. N. Rijal, "Fluorescence Microscope: Principles, Types, and Applications," *Microbe Online* (2022).
38. "Widefield Fluorescence Microscopy," *Ibidi Gmbh* (2023).
39. E. M. C. Hillman, V. Voleti, W. Li, and H. Yu, "Light-Sheet Microscopy in Neuroscience," *Annu. Rev. Neurosci.* **42**: 295-313 (2019).
40. T. H. Chen, J. T. Ault, H. A. Stone, and C. B. Arnold, "High-speed axial-scanning wide-field microscopy for volumetric particle tracking velocimetry," *Exp. Fluids.* **58**(5): 41 (2017).
41. Z. Chen, et. al., "High-Speed Large-Field Multifocal Illumination Fluorescence Microscopy," *Laser Photonics Rev.* **14**: (2019).
42. A. Mau, K. Friedl, C. Leterrier, N. Bourg, and S. Lévêque-Fort, "Fast widefield scan provides tunable and uniform illumination optimizing super-resolution microscopy on large fields," *Nat. Commun.* **12**(1): 3077 (2021).
43. J. P. Nguyen, et. al., "Whole-brain calcium imaging with cellular resolution in freely behaving *Caenorhabditis elegans*," *PNAS.* **113**(8): E1074-E1081 (2015).
44. V. Voleti, et. al., "Real-time volumetric microscopy of in vivo dynamics and large-scale samples with SCAPE 2.0," *Nat. Methods.* **16**(10): 1054-1062 (2019).
45. J. L. Fan, et. al., "High-speed volumetric two-photon fluorescence imaging of neurovascular dynamics," *Nat. Commun.* **11**: 6020 (2020).

46. C. Martin, et. al., "Line excitation array detection fluorescence microscopy at 0.8 million frames per second," *Nat. Commun.* **9**(1): 4499 (2018).
47. "The Grating Equation," *Newport Corp.* (2023).
48. K. Podgorski, and G. Ranganathan, "Brain heating induced by near-infrared lasers during multiphoton microscopy," *J. Neurophisiol.* **116**(3): 1012-1023 (2016).
49. K. Takasaki, R. Abbasi-Asl, and J. Waters, "Superficial Bound of the Depth Limit of Two-Photon Imaging in Mouse Brain," *eNeuro.* **7**(1): (2019).